Aerodynamic Performance Analysis of C-wing Configurations

Undergraduate Thesis

Presented in Partial Fulfillment of the Requirements for Graduation with Distinction in the Department of Mechanical and Aerospace Engineering at The Ohio State University

By

Jordan Douglas Stechschulte

Undergraduate Program in Aeronautical and Astronautical Engineering

The Ohio State University

May 2020

Undergrad Examination Committee:

Dr. Clifford A. Whitfield, Advisor, Ph.D.

Dr. Richard J. Freuler, Ph.D.

Abstract

This thesis investigates the aerodynamic performance of a C-wing. The primary goal of this study was to investigate how the vertical length, horizontal length, and sweep angle of the wing affect the performance of the C-wing. The performance characteristics for each wing were simulated using vortex lattice method in OpenVSP. OpenVSP was run using a wing with known data to determine appropriate settings and panel size. It was concluded that the change in coefficient of lift, drag, and lift-to-drag ratio of the wing changed relatively linearly as the size of the C-wing increased. It was also found that changing the sweep angle of the vertical section had very little effect on the performance as the sweep angle was increased and changing the sweep angle dynamically in flight could be used to control the aircraft. It was also concluded that the C-wing had a locally ideal performance range for coefficient of lift, drag, and lift-to-drag ratio when the vertical length was 12-17% and the horizontal length was less than 12%.

Dedication

To my family, friends, and advisor for helping to make this thesis possible.

Acknowledgments

I would like to thank and express my gratitude to Dr. Clifford A. Whitfield, Ph.D. for his guidance and help throughout this research and my undergraduate career. I am very grateful for his willingness to mentor me through this process. He is an excellent mentor and has also shows great excitement in helping me and many other students at The Ohio State University to learn and understand many topics related to aerospace.

I would also like to thank my committee member Dr. Richard J. Freuler, Ph.D. for his time on helping me in the final stages of my thesis.

A very special thanks to my best friend and girlfriend for their constant support and encouragement for me to do my best.

Finally, I would like to thank my family and friends for their support through my undergraduate career.

Table of Contents

List of Figures

Chapter 1: Introduction

1.1 Introduction

Air travel continues to grow each year, and the trend does not appear to be slowing down as the FAA projects that the global air travel will increase between 1.3-2.5% per year from 2019 to 2039 [1]. This increases the need for more efficient aircraft to help decrease the environmental impacts of air travel as increased fuel usage can deplete nonrenewable resources and increase air pollution. More aerodynamically efficient aircraft will help to increase the range and reduce required fuel cost. The main contributor to aerodynamic inefficiency is the aircraft's drag, which must be overcome by the engines to maintain flight. Most commercial and private aircraft fly in the mid- to high-subsonic flight regimes with Mach numbers less than or on the order of 0.90. The focus of this paper will be in subsonic flight.

For aircraft, and especially transport aircraft, it is important to design a wing configuration that maximizes lift and minimizes drag. In the subsonic flight region, there are two main types of drag that are prominent. The first being the drag at zero lift, this is predominantly due to skin friction and form drag which are primarily affected by the overall size and surface areas of the aircraft components. The second type of drag is induced drag, or drag due-to-lift, and is primarily affected by the shape of the wing. The cause for induced drag is wing tip vortices which can be seen in Figure 1. The wing tip vortices are formed when high-pressure air from the underside of the wing flows around the wing tip to the low-pressure air on the top side of the wing. This causes drag in three main ways: 1) causes the pressure gradient to change; 2) it changes the lift vector direction due to the downwash; and 3) it adds rotational kinetic energy to the flow [2]. For subsonic flow, induced drag is the predominant component of the drag from the wing.

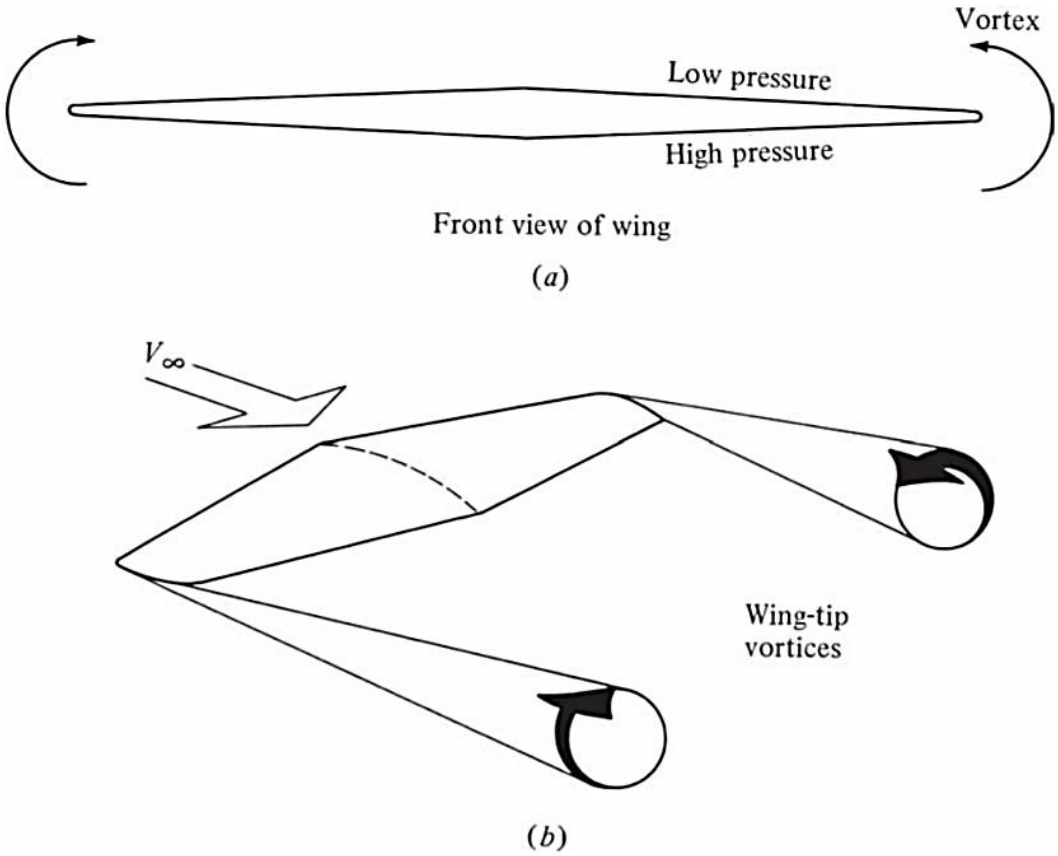

Figure 1: Wing Tip Vortices [2]

The conventional way that induced drag has been reduced is through changing the wing tip, as seen in Figure 2. Winglets can offer substantial reduction in induced drag; however, they do have some draw backs. One disadvantage is that they add weight to the tip of the wing and can potentially increase wing flutter. Another disadvantage is that winglets are typically designed for a very specific flight velocity. For these reasons, winglets are often designed for already existing aircraft wings that need an increase in performance. [3]

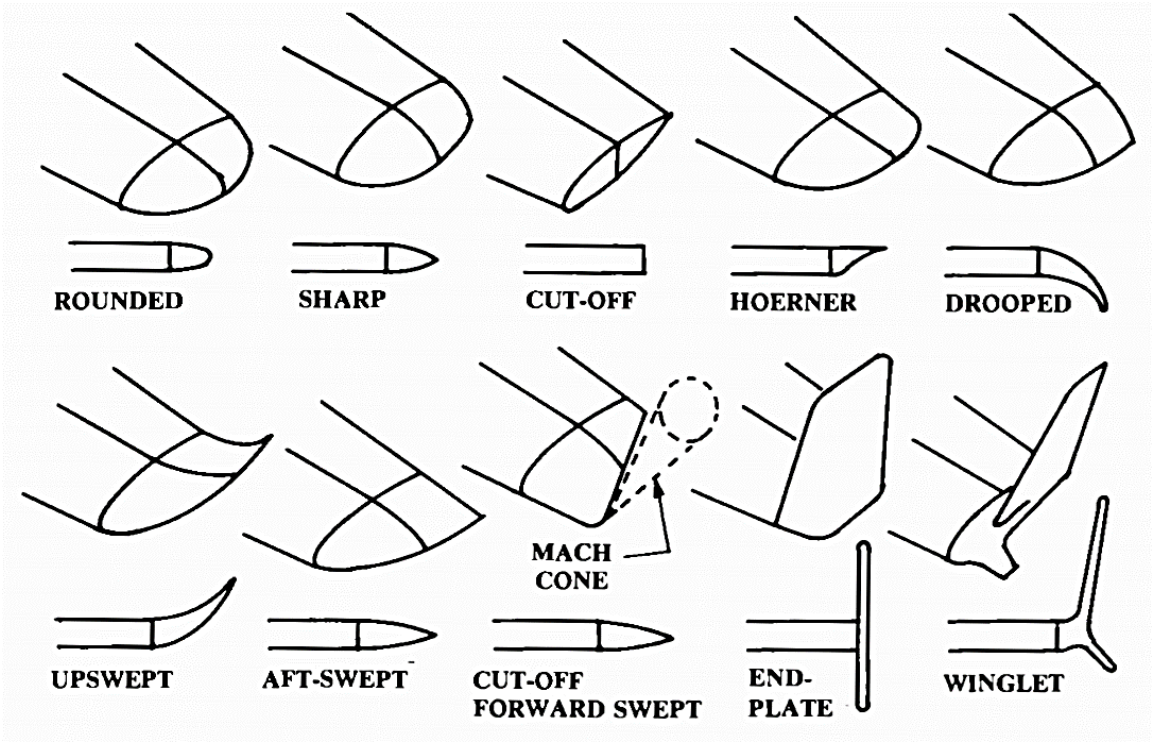

Figure 2: Wing Tips [3]

In the conceptual design phase, computer-aided engineering tools are used to gain an understanding of how different candidate aircraft layouts will perform and how possible design changes will impact the aerodynamic characteristics of the aircraft. The low-order computer-aided tools typically do not take a substantial amount of computation time or resources. This supports large number of changes to the shape of the aircraft, to determine how design changes affect the aircraft. This allows for the testing of new or previously untested ideas to study their effects on aircraft.

Kroo provides some examples of possible novel wing designs that could reduce the induced drag, separate from winglets, with one of the most promising designs that is highlighted is a C-wing [4]. Kroo indicates that a C-wing provides almost the same efficiency as a box wing, without as many of the penalties that the box wing incurs. This can be seen in Figure 3, where a C-wing that extends over the wing only 10% has an efficiency that is within approximately 1% of the efficiency of the box wing [4]. This concept provides an opportunity to conduct further conceptual design research studies.

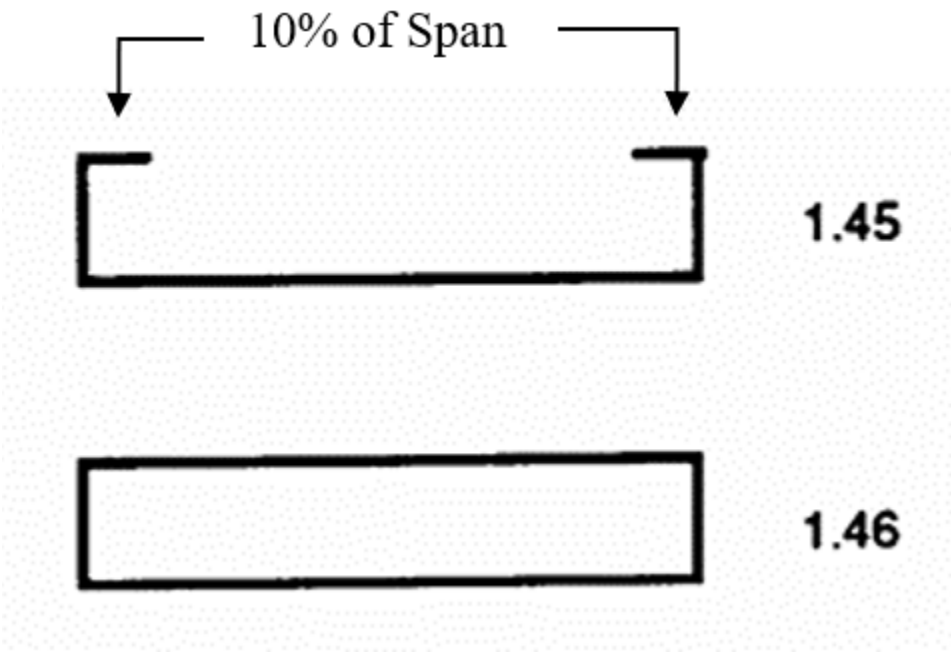

Figure 3: Span Efficiency for C-wing and Box Wing Hight/Span = 0.2 [4]

In the conceptual design phase, computational fluid dynamics (CFD) is used to model and solve the flow field around an aircraft. Simplified CFD solvers are commonly used, and some of the assumptions made to help reduce the complexity are irrotational flow and inviscid flow. One simplified method involves using the vortex lattice method (VLM). Using this approach to solve the flow field around an aircraft helps to draw conclusions on how the aircraft may perform, which can later be tested and verified by higher order CFD simulations, and experimental testing.

1.2 Background

This section gives an overview of the relevant fluid mechanics of inviscid subsonic flow, the use of CFD VLM to solve flows for C-wing, and previous relevant work to C-wing aerodynamics.

1.2.1 Overview Subsonic Flows for Wings

For subsonic air flow, there are several assumptions that can be made to simplify analyzing the flow around a wing. The first assumption assumes that the flow is inviscid. With inviscid flow, the flow neglects friction. The second assumption assumes that the flow is steady. Steady flow assumes that mass flow from cross section one to cross section two along flow streamlines, as seen in Figure 4, remains the same. This assumption means that flow does not cross streamlines. The third and final assumption assumes that the flow is incompressible and the density throughout the flow-field remains the same. These assumptions are valid for flow speeds approximately Mach 0.3 or less. With these assumptions, the flow is considered inviscid, steady, and incompressible [2].

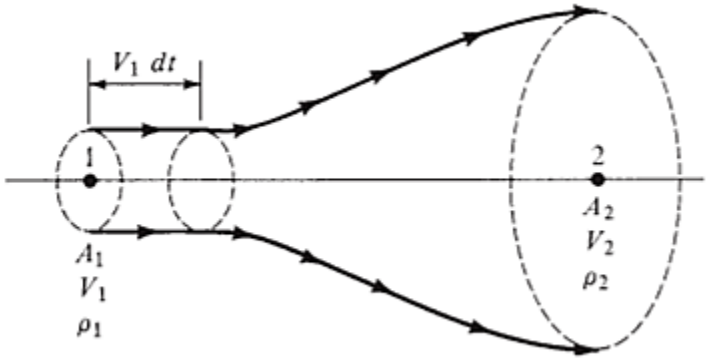

Figure 4: Stream Tube [2]

1.2.2 Vortex Lattice Method

For inviscid airflow, VLM is a simple and easy tool to use to analyze the aerodynamic performance of a wing. VLM works by splitting a surface into panels with a control point at the center of every panel, and the velocity induced at each control point is summed giving a set of linear algebraic equations. To calculate the velocity at each control point, a horseshoe vortex is placed around each panel, as seen in Figure 5.

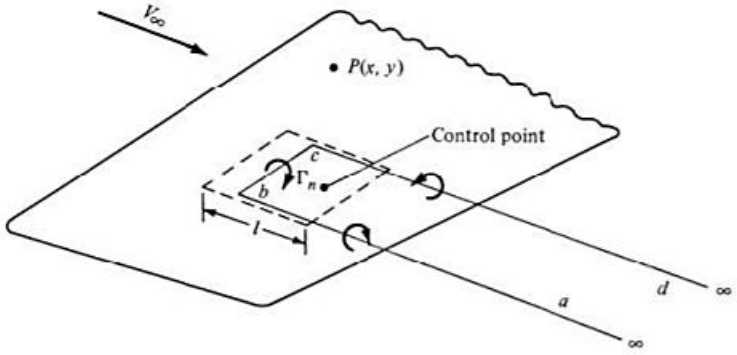

Figure 5: Horseshoe Vortex [6]

The linear equation obtained by summing up the control points is used to calculate the strength of the horseshoe vortices. Boundary conditions are applied to ensure that no flow is moving through the wing. The total forces and moments of the wing are then calculated by integrating the pressure differential of the upper and lower part of the wing caused by the vortices [5]. To calculate the velocity caused by each horseshoe vortex on a control point, Equations 1.1–1.3 are used. Equation 1.1 represents the velocity induced by the vertex section (b)-(c) in Figure 5, Equation 1.2 represents vortex section (b)-(a) when (a) goes to infinity in Figure 5, and Equation 1.3 represents the vortex section (c)-(d) when (d) goes to infinity in Figure 5.

$$\overrightarrow{V_{bc}} =$$

$$\frac{\Gamma_n}{4\pi}\left\{\frac{\{[(y_m-y_{1n})(z_m-Z_{2n})-(y_m-y_{2n})(z_m-z_{1n})]\hat{\imath}-[(x_m-x_{1n})(z_m-z_{2n})-(x_m-x_{2n})(z_m-z_{1n})]\hat{\jmath}+[(x_m-x_{1n})(y_m-y_{2n})-(x_m-x_{2n})(y_m-y_{1n})]\hat{k}\}}{\{[(y_m-y_{1n})(z_m-Z_{2n})-(y_m-y_{2n})(z_m-z_{1n})]^2+[(x_m-x_{1n})(z_m-z_{2n})-(x_m-x_{2n})(z_m-z_{1n})]^2+[(x_m-x_{1n})(y_m-y_{2n})-(x_m-x_{2n})(y_m-y_{1n})]^2\}}\right.$$

$$\left\{\frac{[(x_{2n}-x_{1n})(x_m-x_{1n})+(y_{2n}-y_{1n})(y_m-y_{1n})+(z_{2n}-z_{1n})(z_m-z_{1n})]}{\sqrt{(x_m-x_{1n})^2+(y_m-y_{1n})^2+(z_m-z_{1n})^2}}-\right.$$

$$\left.\frac{[(x_{2n}-x_{1n})(x_m-x_{2n})+(y_{2n}-y_{1n})(y_m-y_{2n})+(z_{2n}-z_{1n})(z_m-z_{2n})]}{\sqrt{(x_m-x_{2n})^2+(y_m-y_{2n})^2+(z_m-z_{2n})^2}}\right\} \qquad (1.1)$$

$$\overrightarrow{V_{ba}} = \frac{\Gamma_n}{4\pi}\left\{\frac{(z_m-z_{1n})\hat{\jmath}+(y_{1n}-y_m)\hat{k}}{[(z_m-z_{1n})^2+(y_{1n}-y_m)^2]}\right\}\left[1+\frac{x_m-x_{1n}}{\sqrt{(x_m-x_{1n})^2+(y_m-y_{1n})^2+(z_m-z_{1n})^2}}\right] \qquad (1.2)$$

$$\overrightarrow{V_{cd}} = -\frac{\Gamma_n}{4\pi}\left\{\frac{(z_m-z_{2n})\hat{\jmath}+(y_{2n}-y_m)\hat{k}}{[(z_m-z_{2n})^2+(y_{2n}-y_m)^2]}\right\}\left[1+\frac{x_m-x_{2n}}{\sqrt{(x_m-x_{2n})^2+(y_m-y_{2n})^2+(z_m-z_{2n})^2}}\right] \qquad (1.3)$$

In these equations, Γ_n represents the nth vortices strength, (x_m, y_m, z_m) represent the location of the mth control point, (x_{1n}, y_{1n}, z_{1n}) represent the first corner point of the nth horseshoe vortex, point (b) in Figure 5, and (x_{2n}, y_{2n}, z_{2n}) represents the second corner point of the nth horseshoe vortex, point (c) in Figure 5. Once Equations 1.1-1.3 are summed together, the velocity induced by the nth horseshoe vortex for the mth control point is determined. Then once the velocity induced by all horseshoe vortices for the mth control point are added up, the total velocity at control point m is determined by Equation 1.4.

$$\overrightarrow{V_m} = \sum_{n=1}^{2N} \overrightarrow{C_{m,n}}\,\Gamma_n \qquad (1.4)$$

$\overrightarrow{C_{m,n}}$ is a coefficient that depends on the geometry of the horseshoe vortex and its distance from the control point. From Equation 1.4 a linear equation is obtained by adding the velocity induced by the 2N vortices on the mth control point. Since there are also 2N control points, a 2Nx2N matrix is made. This matrix is then solved to find the induced velocity at each control point for all determined vortices strengths using the boundary conditions on the wing [5].

The equation for the boundary conditions are shown below in Equation 1.5. This equation needs to be solved for every control point resulting in a 2N vector with the unknown vortices strengths required to satisfy these conditions. This is done by simultaneously solving the matrices given by Equation 1.4 and Equation 1.5. In Equation 1.5, ω_m represents the downwash velocity at control point m, v_m represents the vertical velocity at control point m, ϕ represents the dihedral angle of the wing, U represents the flow velocity at infinity, α represents the angle of attack, and $\left(\frac{dz}{dx}\right)_m$ represents the slope of the mean camber line at control point m. Equation 1.5 also assumes a small slope of the mean cambered line and small angles of attack [5].

$$\omega_m - v_m \tan(\phi) + U\left[\alpha - \left(\frac{dz}{dx}\right)_m\right] = 0 \qquad (1.5)$$

1.2.3 C-wing Design and Aerodynamic Characteristics

The C-wing design has been shown to be a possible solution to help increase the aerodynamic efficiency of an aircraft. The increased efficiency of the C-wing comes from two major components of its design. First, it helps to control wing tip vortices. Second, it adds a second lifting surface to the wing [4]. Gage developed a genetic algorithm with minimized induced drag as the parameter to which the algorithm was to optimize. The algorithm came up with a C-wing as being the most optimal wing design [7]. Both Kroo and Gage showed that a C-wing has similar performance to the box wing [4]. Their research provides a foundation to study the aerodynamic performance of a C-wing in more depth, and how changing the shape of the C-wing affects overall performance.

1.3 Motivation and Overview

The motivation for this research was to better understand the aerodynamic characteristics of a C-wing and how changing its shape affects its performance. The main objectives of this paper were to use a VLM solver to 1) understand how the height of the C-wing; 2) how the length that it extends back over the wing; and 3) how the sweep of the C-wing all affect its aerodynamic performance. Finally, from the aerodynamic performance of the C-wing, parametric trade studies were conducted to assist in meeting the objectives of how a C-wing would help the performance of an aircraft.

This paper will be broken up into five chapters. A literature review on C-wings and an overview of VLM and C-wings was given in this first chapter. The second chapter will discuss OpenVSP and how the computational results were verified and validated. The third chapter covers the VLM results of the C-wing and are discussed. In the fourth chapter, the results from the trade study are presented and discussed. In the fifth and final chapter conclusion, remarks, and future work is discussed.

Chapter 2: OpenVSP Panel Sensitivity Study

This chapter will discuss the steps taken to validate the results from OpenVSP and wing configurations.

2.1 Baseline Wing in OpenVSP

OpenVSP was run using the VLM solver. The results were compared to estimations of the lift coefficient using the 2D airfoil data and standard 3D wing estimation techniques [2]. For this research, a NACA 64-006 airfoil was chosen, and a rectangular wing with an aspect ratio of 8.0 was used as the baseline wing for VLM setup verifications using OpenVSP.

To obtain the lift curve slope for the 2D airfoil, the slope was determined from experimental data [8]. Using a Reynolds number of 6 million, the slope was determined as 0.10 per degree as seen in Figure 6.

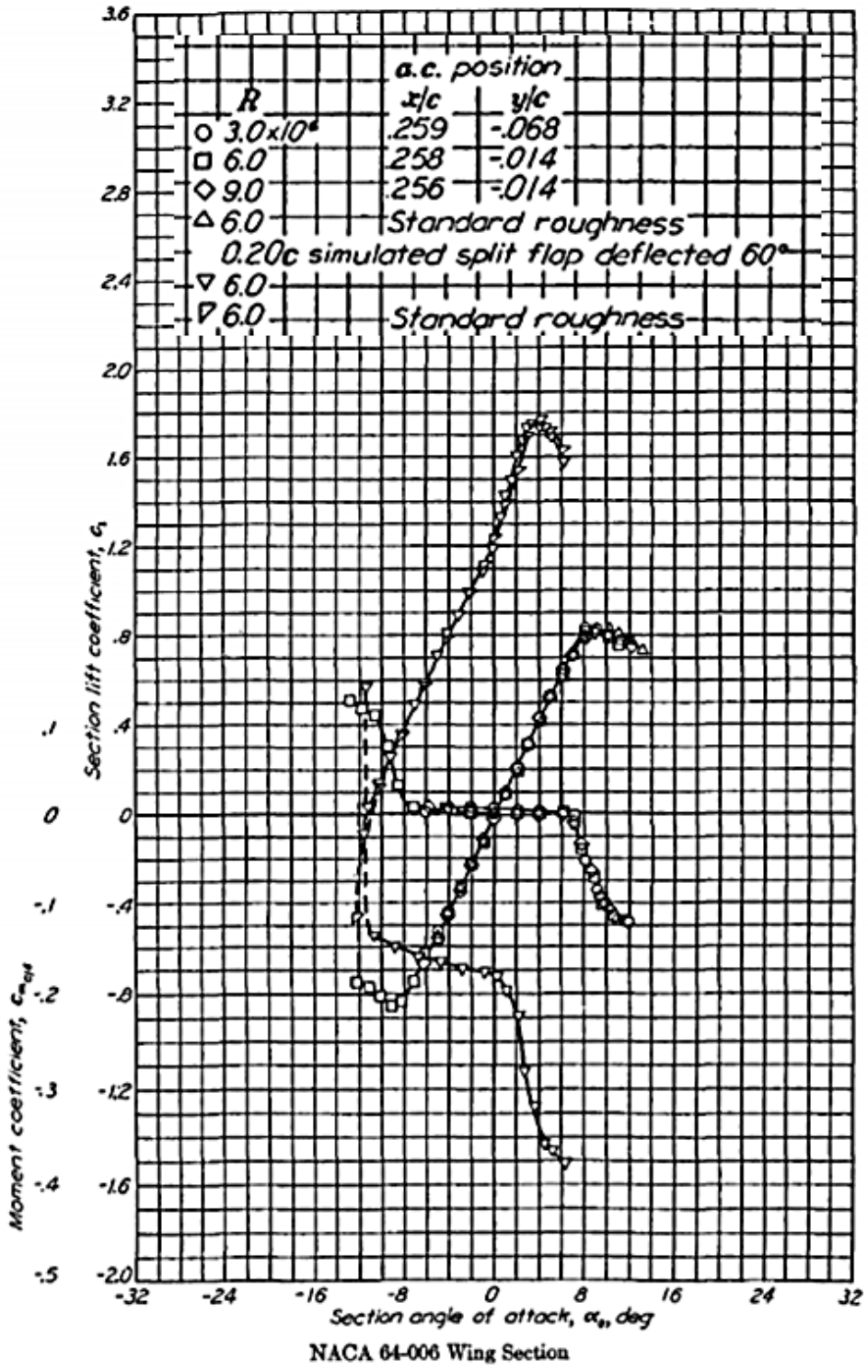

Figure 6: Lift Curve Slops for NACA64-006 [7]

This lift curve slope and Equation 2.1 were used to estimate a span wise efficiency factor of 0.77. Using Equation 2.2, the 3D lift curve for the wing was estimated to be 0.080 per degree.

$$e = \frac{1}{\pi * AR * r + 1 + \delta} \qquad (2.1)$$

$$\alpha_{3D} = \frac{\alpha_{2D}}{1 + \frac{57.3 * \alpha_{2D}}{\pi * AR * e}} \qquad (2.2)$$

In the equations above, the coefficient e is the span wise efficiency factor, AR is the aspect ratio, α_{3D} is the lift curve slope for the wing, and α_{2D} is the lift curve slope for the airfoil. The constants r and δ are estimated from empirical data. For the designed wing, r was estimated to be on the order of 0.009, and δ was estimated to be 0.085 from the data shown below in Figure 7.

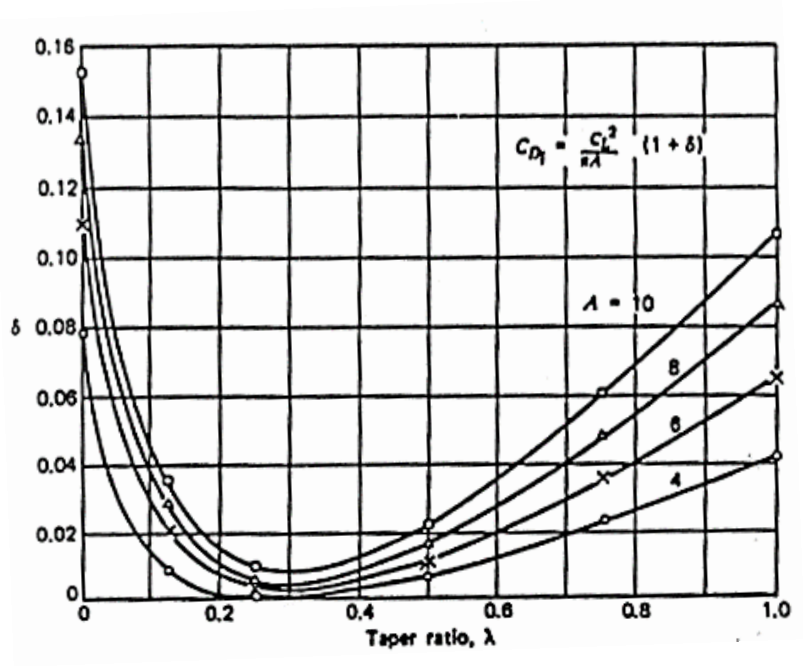

Figure 7: Induced Drag factor δ

.

As seen in figure 8, the 2D lift curve slope is greater than the 3D lift curve slope. The decrease in lift curve slope is due to the formation of wing tip vortices. The wing tip vortices cause downwash, changing the effective angle-of-attack of the wing by rotating the airflow around the wingtip. This causes the incoming airflow to be at a slightly different angle than the freestream airflow. Thus, care must be taken when setting up the simulation to properly simulate this complex airflow around the wing tip. The panel distribution is one of the most influential factors for accuracy in the results, and determining an ideal panel distribution is very important.

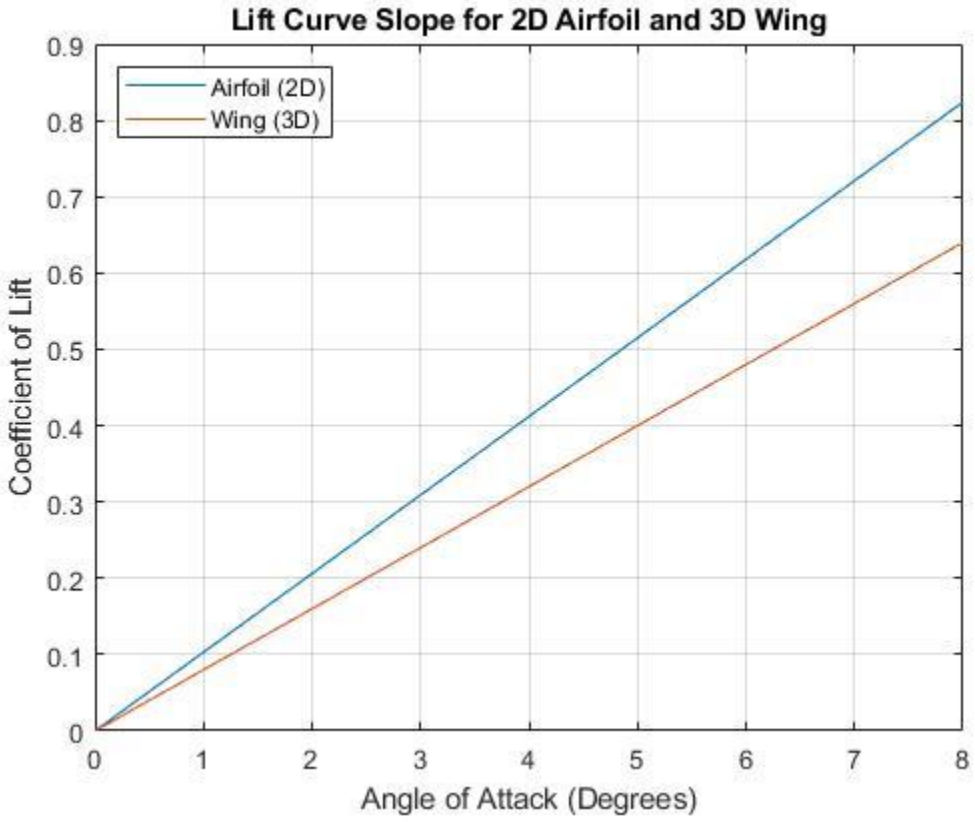

Figure 8: 2D and 3D lift curve for rectangle wing

After the empirically-driven analytical 3D lift curve slope was obtained, a wing panel sensitivity study was performed. This study was performed to determine the sensitivity of the lift curve slope to the panel distribution and number of panels used in OpenVSP VLM solver for a rectangular wing. For the panel sensitivity test on the rectangular wing the Mach number was set to 0.1 at standard sea level conditions. All settings in OpenVSP were kept constant except for the number and distribution of wing surface panels. First considered was determining the sensitivity of the results due to changes of panel size in the chord-wise direction from 8.33% to 1.38% of the overall chord. The panel sizes in the wingspan direction were kept constant at 4.5% of the overall wingspan. The results are provided in Figure 9.

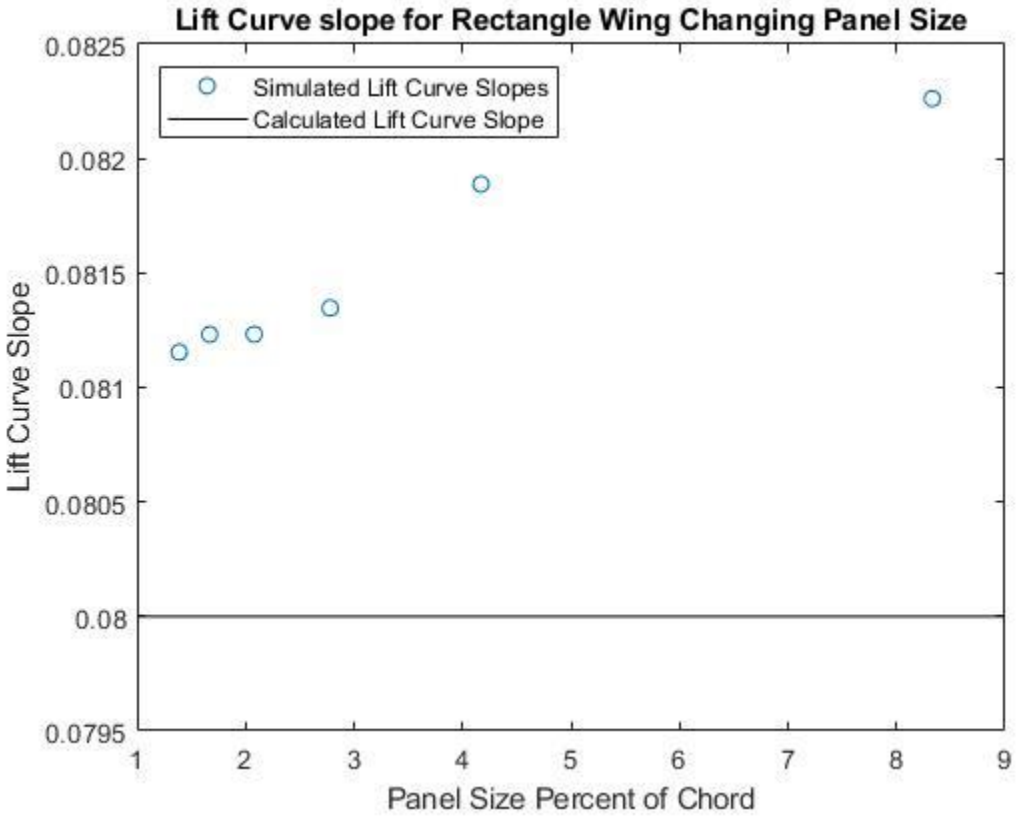

Figure 9: Rectangle Wing Chord Panel Size Study

It is observed in Figure 9 that once the panel size reaches a size smaller than 2.78% in the chord-wise direction, the lift curve slope changes by less than 0.14%, a threshold that was determined to be reasonable for this C-wing geometric comparative study. Decreasing the chord-wise panel size significantly impacted the computation time with very little impact on the predicted results.

After the chord-wise panel sizing was determined, additional testing was completed for the wingspan panel size. The panel changes for this study can be seen in Figure 10 which shows the two extreme ends of the panel sizes tested. The top wing in Figure 10 has panel sizes that correspond to 4.55% of the wingspan, the largest panel size, and the bottom wing has panel sizes that correspond to 0.60% of the wingspan, the smallest panel size. The chord-wise panel sizing is 2.78% of the chord for all runs.

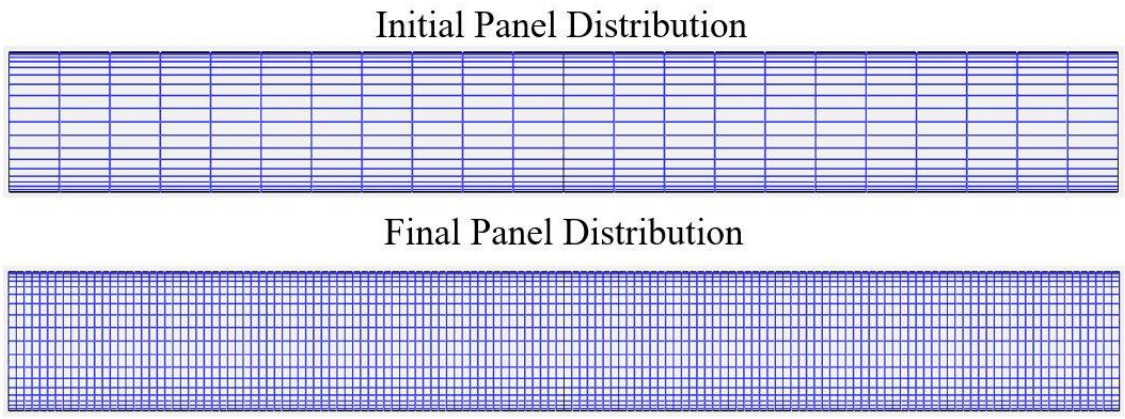

Figure 10: Panel Sizes

The results of the span-wise panel distribution sensitivity study are provided below in Figure 11. The results show that for panels smaller than 0.85% of the wingspan, the predicted lift curve slope values converge. Based on the results, a final panel size of 0.70% of the wingspan was set for the C-wing study.

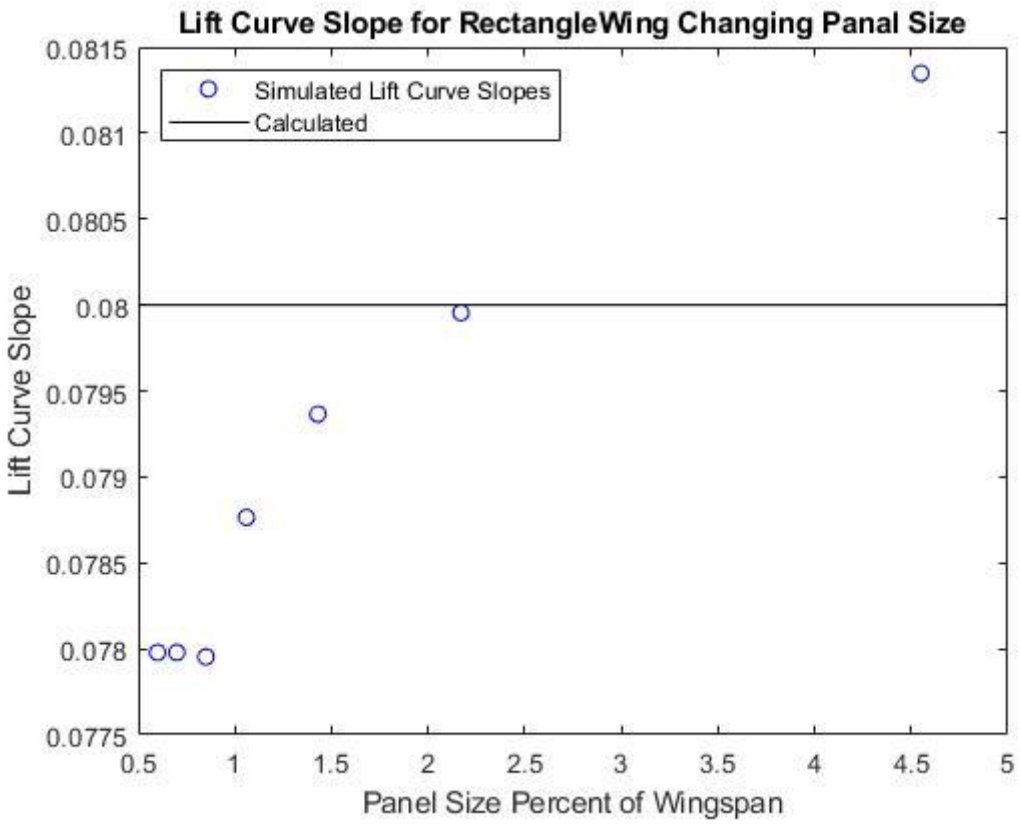

Figure 11: Rectangle Wing Wingspan Panel Size Study

The Mach number and Reynolds number are important dimensionless parameters in aerodynamics and are commonly referred to as similarity parameters. Reynolds number is a measurement of the ratio of inertia force to viscous force, and Mach number is the ratio of velocity to speed of sound of a flow [6]. Similarity parameters imply that if Mach number and Reynolds number are consistent for flows over two similar geometries that are scaled differently, the aerodynamic results will have similar characteristics. Mach number and Reynolds number are correlated through the flow's velocity. Using the calculated lift curve slope for the wing, and the information gathered in the panel sensitivity test to obtain the panel sizing, the sensitivity to Mach number in the incompressible range was determined. For the Mach test, all parameters were set to

sea level on a standard day. The Mach number and Reynolds number can be determined using Equations 2.3 and 2.4:

$$u = M * \sqrt{\gamma * R * T} \qquad (2.3)$$

$$Re = \frac{\rho * u * L}{\mu} \qquad (2.4)$$

In the equations, M represents the Mach number, γ ratio of specific heat, R specific gas constant, T temperature, u velocity, ρ density, L characteristic length, μ dynamic viscosity, and Re the Reynolds number. Setting the desired Mach number, the flow velocity was determined using Equation 3 along with the corresponding Reynolds number from Equation 4. At sea level, the ratio of specific heat for air is 1.4, specific gas constant for air is 1716.49 $\frac{ft * lb_f}{slug * R^0}$, temperature 518.67 R^0, density $23.77 * 10^{-4} \frac{slug}{ft^3}$, and dynamic viscosity $3.737 * 10^{-7} \frac{slug}{ft * s}$. The characteristic length is the wing chord, which was set at 3 ft for this study. The results of the Mach number sensitivity study are provided in Figure 12.

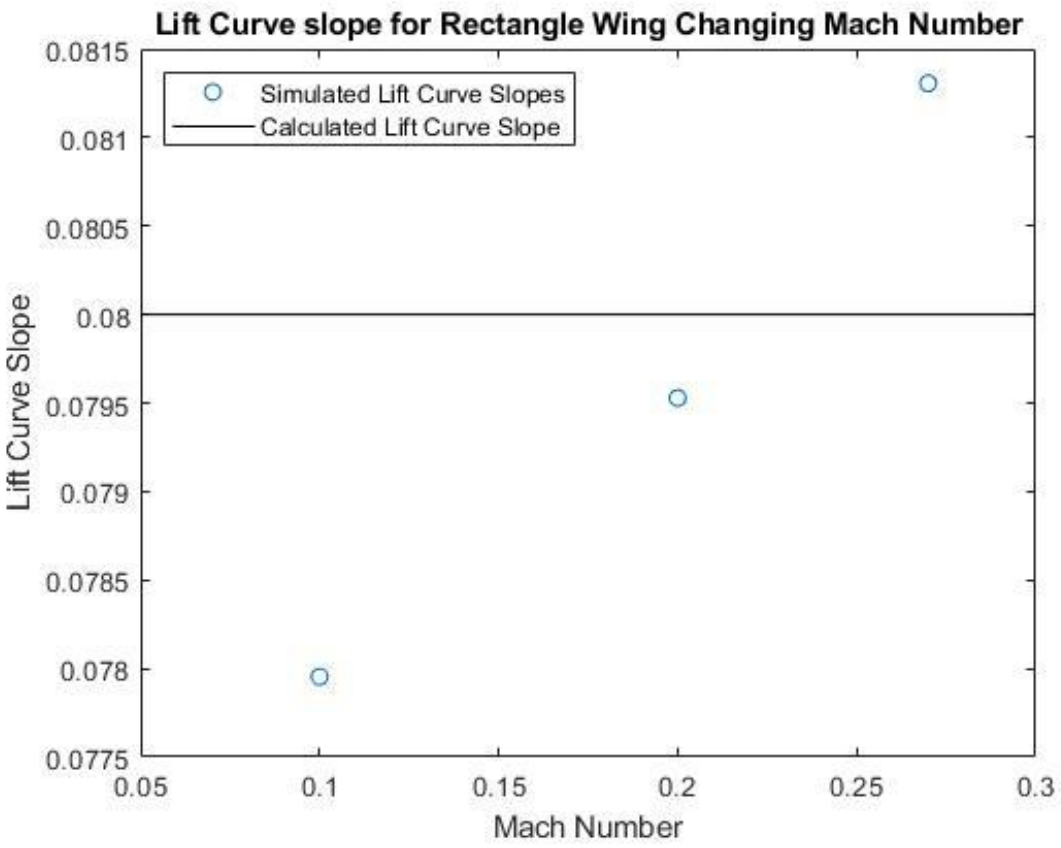

Figure 12: Rectangle Wing Mach Test

The Mach number of 0.2 gives a lift curve slope of 0.0796 which is 0.05% below the calculated lift curve slope line in Figure 12. The Mach number of 0.27 has a lift curve slope of 0.0813 which is 1.63% above the calculated lift curve slope line in Figure 12. The Reynolds number for Mach number 0.2 was calculated to be 4.3 million which is 28.33% off the target Reynolds number of 6 million. The Reynolds number for Mach number 0.27 was calculated to be 5.8 million which is 3.33% off the target Reynolds number of 6 million. Using the results shown in Figure 12 and the results of Reynolds number, a compromise between the results for Mach number and Reynolds's number was determined. A Mach number of 0.27 was selected for the C-wing studies.

2.2 Baseline Wing with Winglet in OpenVSP

Based on the panel sensitivity study from the baseline wing, the panel distributions used for the sensitivity test were performed with winglets of an aspect ratio of 1.0 installed on the wing tips. This was done to determine how the change in geometry may impact the selected panel sizes from the baseline sensitivity analysis. Consistent with the baseline wing, the first step was to determine the impacts of panel sizes in the chord-wise direction for the winglet by varying the panel size from 2.78% to 0.36% of the overall chord with wingspan panel sizing set at 4.55% of the overall wingspan. The results are shown below in Figure 13.

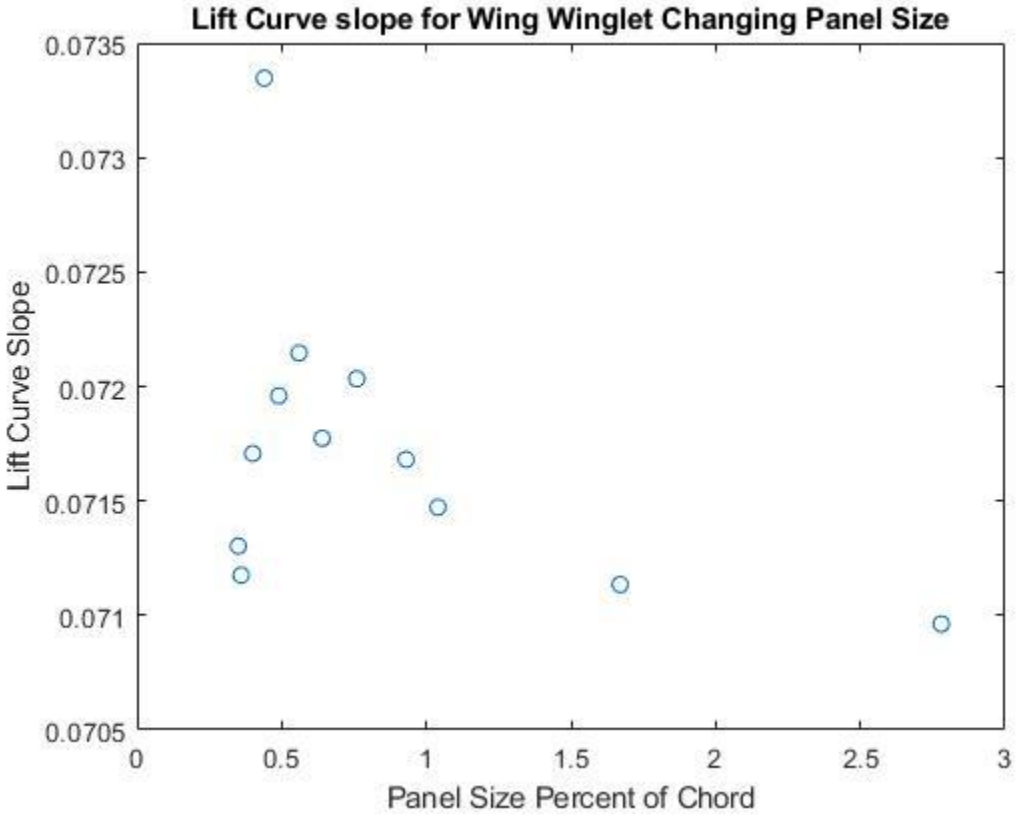

Figure 13: Wing with Winglet Chord Panel Size Study

The results show that new geometry of incorporating a winglet is sensitive to the panel sizing in the chord-wise direction. The panel size of 2.78% of the overall chord was set for the C-wing study. This is consistent from the baseline rectangular wing sensitivity study.

The panel sizing in the wingspan direction of the winglet was also tested. For this test, the panel sizes were varied from 4.55% to 0.60% of the overall wingspan with the chord panel sizing be 2.78% of the overall chord. Figure 14 shows the results of this study. The lift curve slope predictions indicate that as the panel size decreases, the slope continues to decrease. A panel size of 0.70% of the overall winglet span was chosen to maintain consistency with the primary wing's span-wise panel sizes.

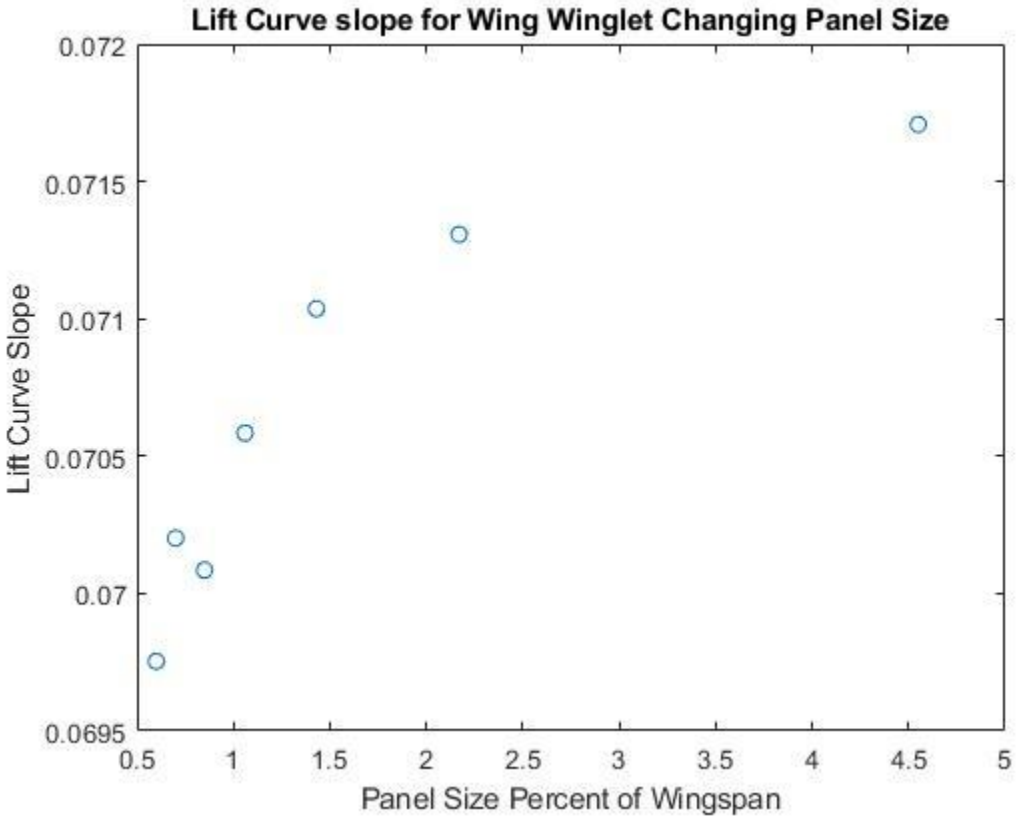

Figure 14: Wing with Winglet Wingspan Panel Size Study

From the studies discussed in this chapter, the setup in OpenVSP and panel distributions on the wing models were determined. Testing conditions would be set to standard sea level conditions, at an incompressible Mach of 0.27, and the panel size was set, based on the sensitivity analyses, to 2.78% of the overall chord and 0.70% of the overall wingspan.

Chapter 3: VLM Results

This chapter will discuss the results and trends in the data between various C-wing geometries obtained from OpenVSP. The first section will discuss the changes in the vertical and horizontal lengths of the C-wing. The second section will discuss the change in the sweep angle of the vertical section of the C-wing.

3.1 Change in Vertical and Horizontal C-wing Size

This section will discuss how the aerodynamic performance of the C-wing changes for variations of horizontal and vertical section lengths. With respect to the half span of the wing, both the horizontal and vertical sections will change from 8.33% to 41.67% with 8.33% steps. A step size of 8.33% was chosen due to its ability to be accounted for in the panel distribution size while also providing a significant amount of points to analyze. Figure 15 shows the forward cross section changes in the C-wing sizes that were studied. In row 1, the horizonal section of the C-wing is at 8.33% and increases to 41.67% at row 5. Across the columns, the vertical section of the C-wing from columns A to E decreases from 41.67% to 8.33%. The baseline wing results from section 2.2 was used as a reference for each test.

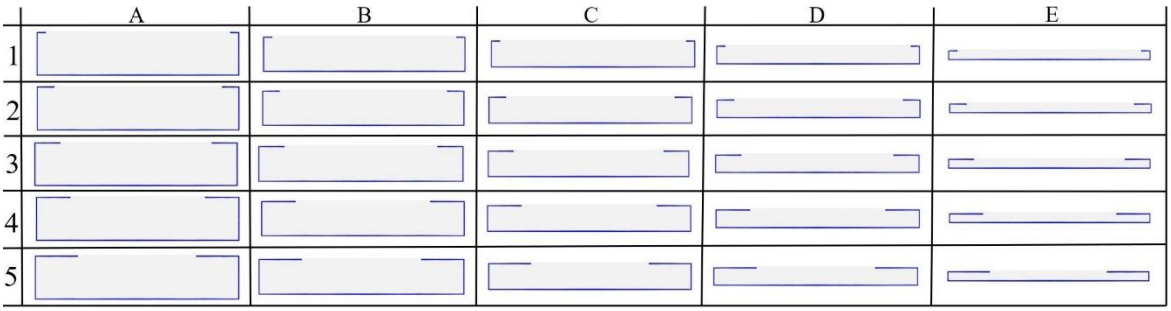

Figure 15: C-wing Sizes

3.1.1 Horizontal C-wing Changes

For the horizontal analysis of the C-wings, the objective was to identify trends for the coefficient of lift and drag and the lift-to-drag ratios while holding the vertical length constant. An angle of attack of seven degrees was chosen for a more in-depth analysis of each wing. The seven-degree angle of attack corresponds to the maximum lift-to-drag ratio for the reference wing. Figures 16-20 show the results, where each figure is split into 6 sub-plots: A) lift curve slope; B) coefficient of lift at the seven-degree angle of attack; C) drag polar; D) coefficient of drag at the seven-degree angle of attack; E) lift-to-drag ratio with respect to angle of attack; and F) lift-to-drag ratio drag at the seven-degree angle of attack.

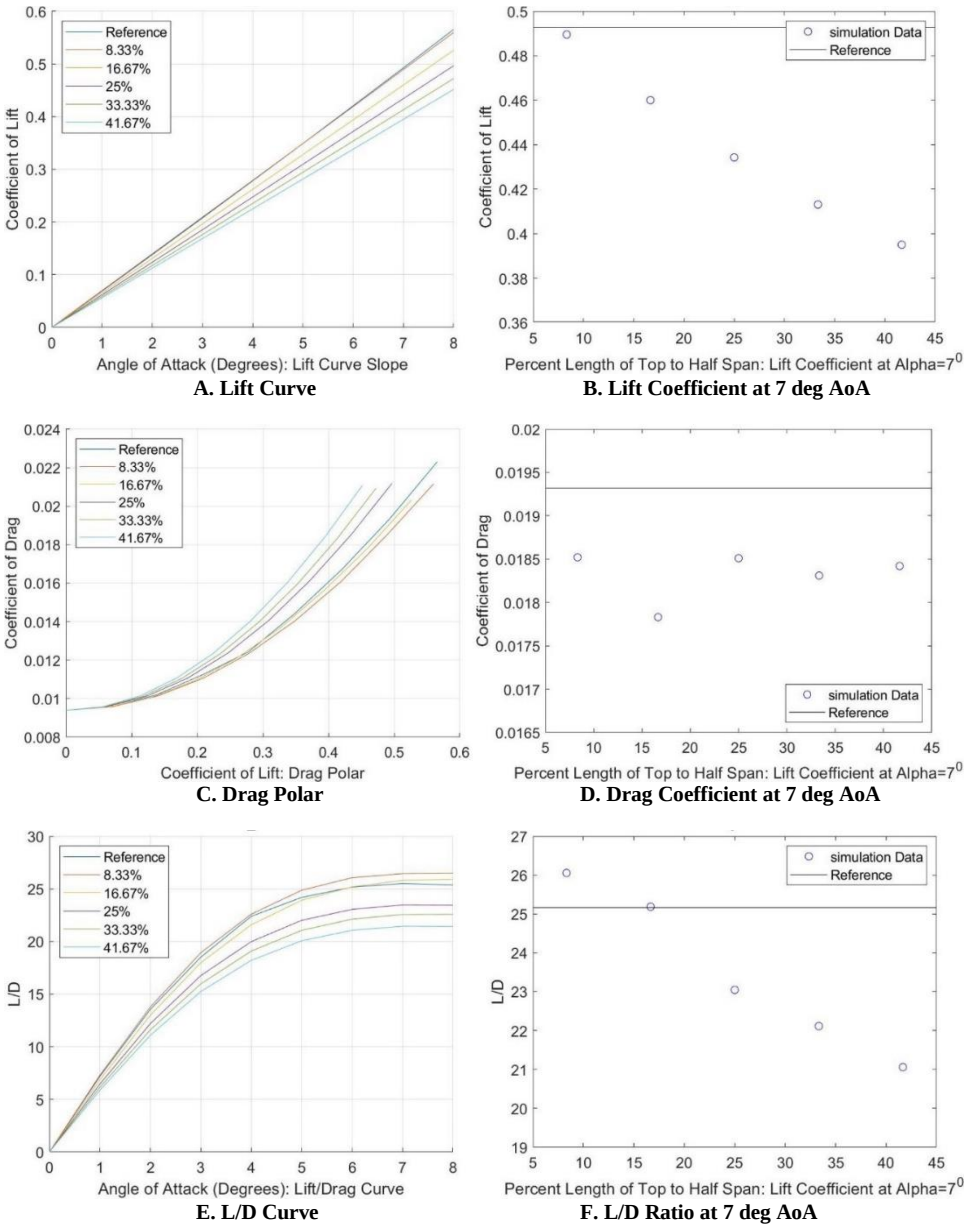

A. Lift Curve **B. Lift Coefficient at 7 deg AoA**

C. Drag Polar **D. Drag Coefficient at 7 deg AoA**

E. L/D Curve **F. L/D Ratio at 7 deg AoA**

Figure 16: C-wing Side 8.33%

Figure 16, sub-plots B and F show that both the lift coefficient and the lift-to-drag ratio decease linearly as the horizontal length increases. Sub-plot D shows the coefficient of drag stays relatively constant except for at a vertical length of 16.67% where there is a sudden decrease.

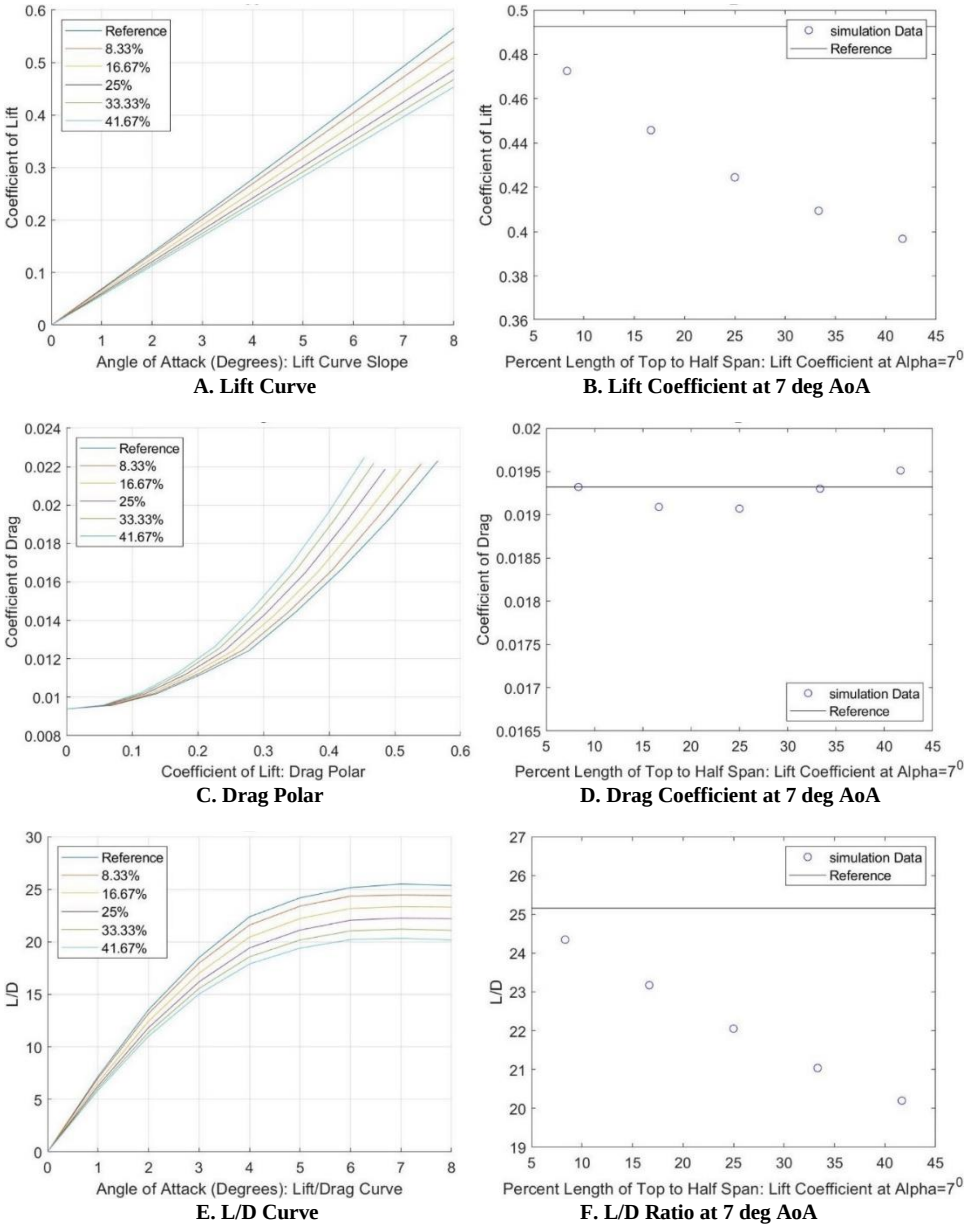

Figure 17: C-wing Side 16.67%

Figure 17, sub-plots B and F show that the coefficient of lift and lift-to-drag ratio decreases linearly. Sub-plot D shows the coefficient of drag change is parabolic starting at the reference value before first decreasing then increasing again as the horizontal length increases.

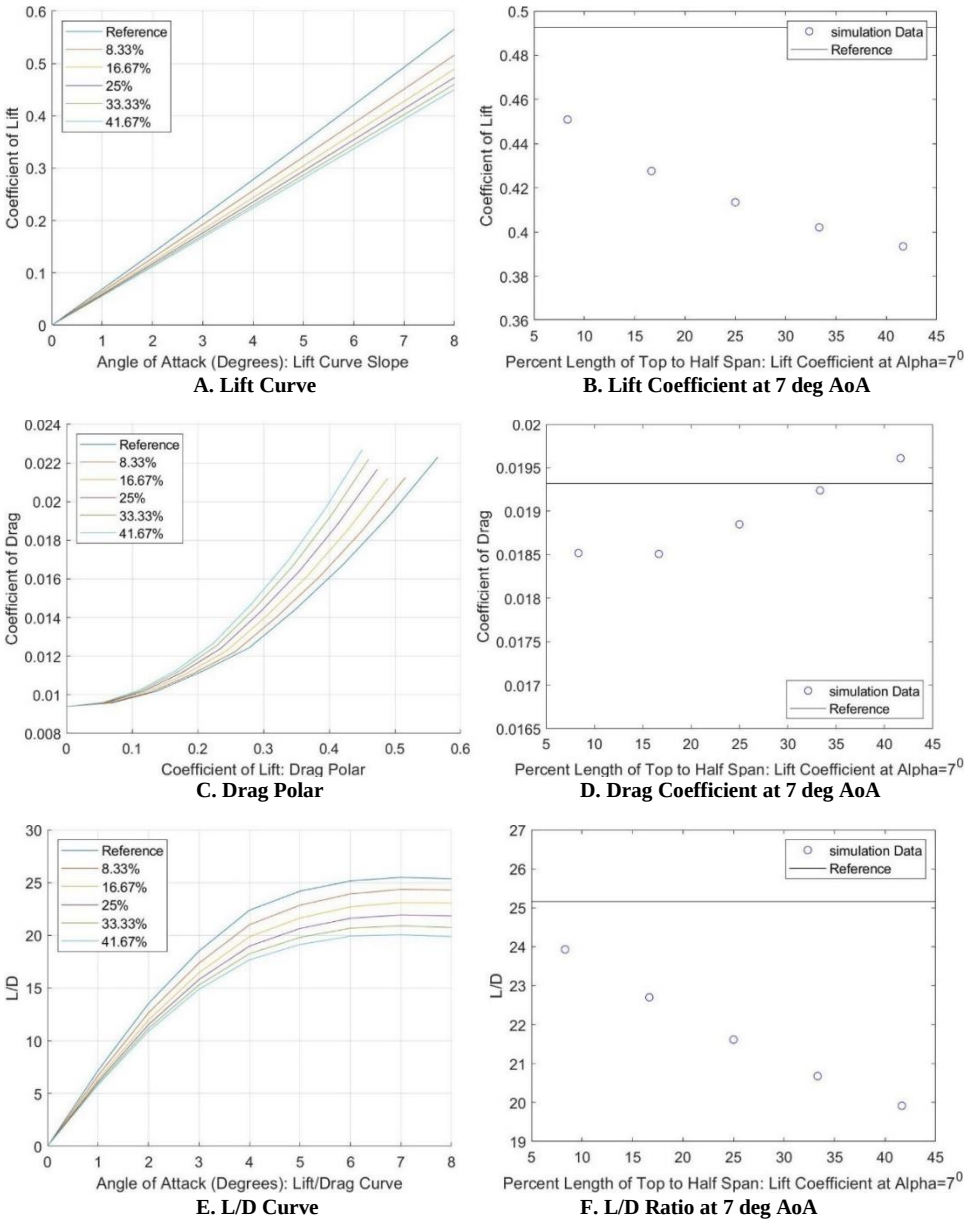

Figure 18: C-wing Side 25%

Figure 18, sub-plots B and F show that the coefficient of lift and the lift-to-drag ratio decreases linearly as the horizontal length increases. Sub-plot D shows the drag coefficient stays the same until a horizontal length of 16.67%. After a horizontal length of 16.67%, the coefficient of drag begins to increase linearly as the horizontal length increases.

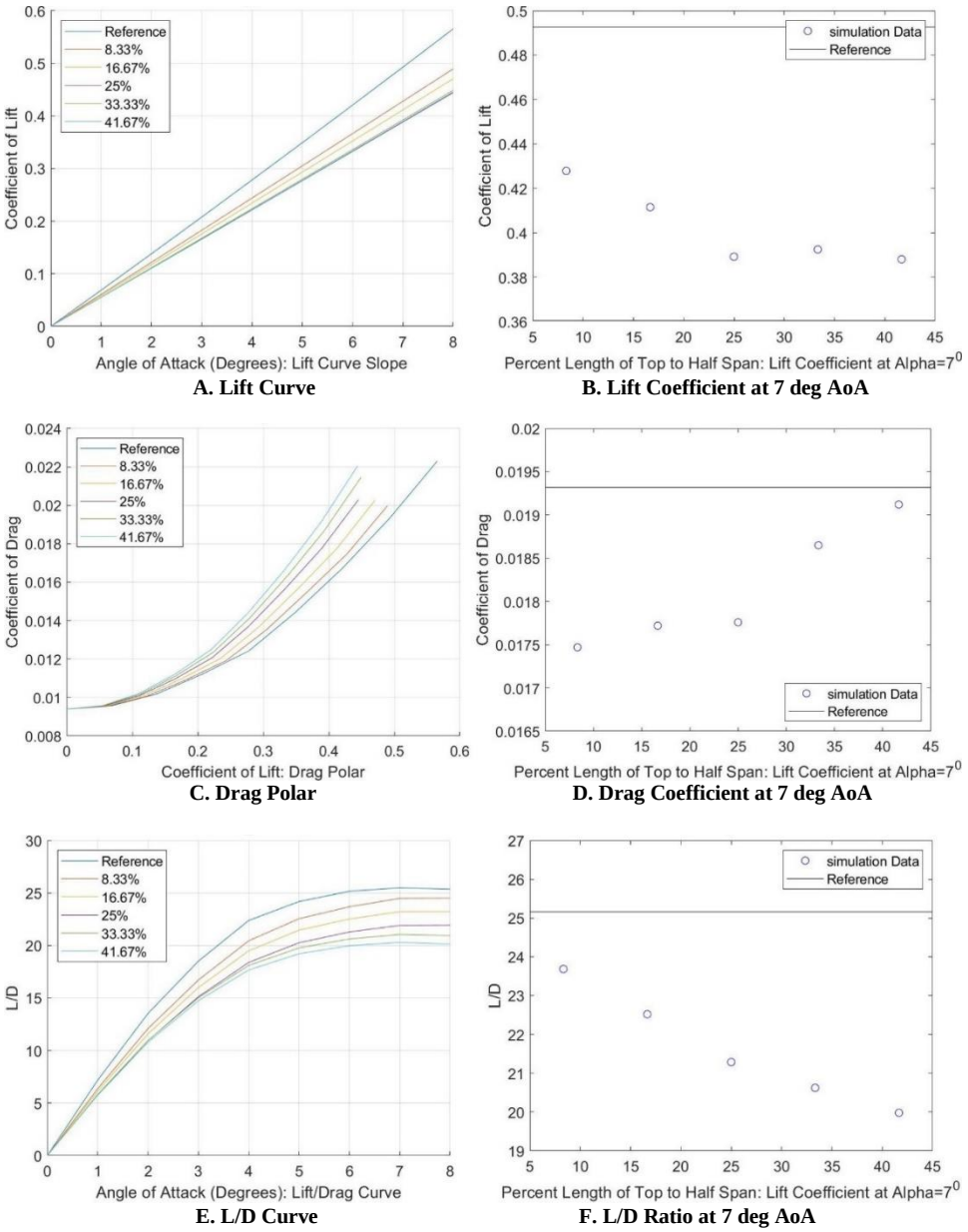

Figure 19: C-wing Side 33.33%

Figure 19, sub-plots B and F show that the coefficient of lift and the lift-to-drag ratio decreases linearly as the horizontal length increases. Sub-plot D shows the coefficient of drag increasing linearly as the horizontal length increases, except between horizontal lengths of 16.67% and 25% where the coefficient of drag remains constant.

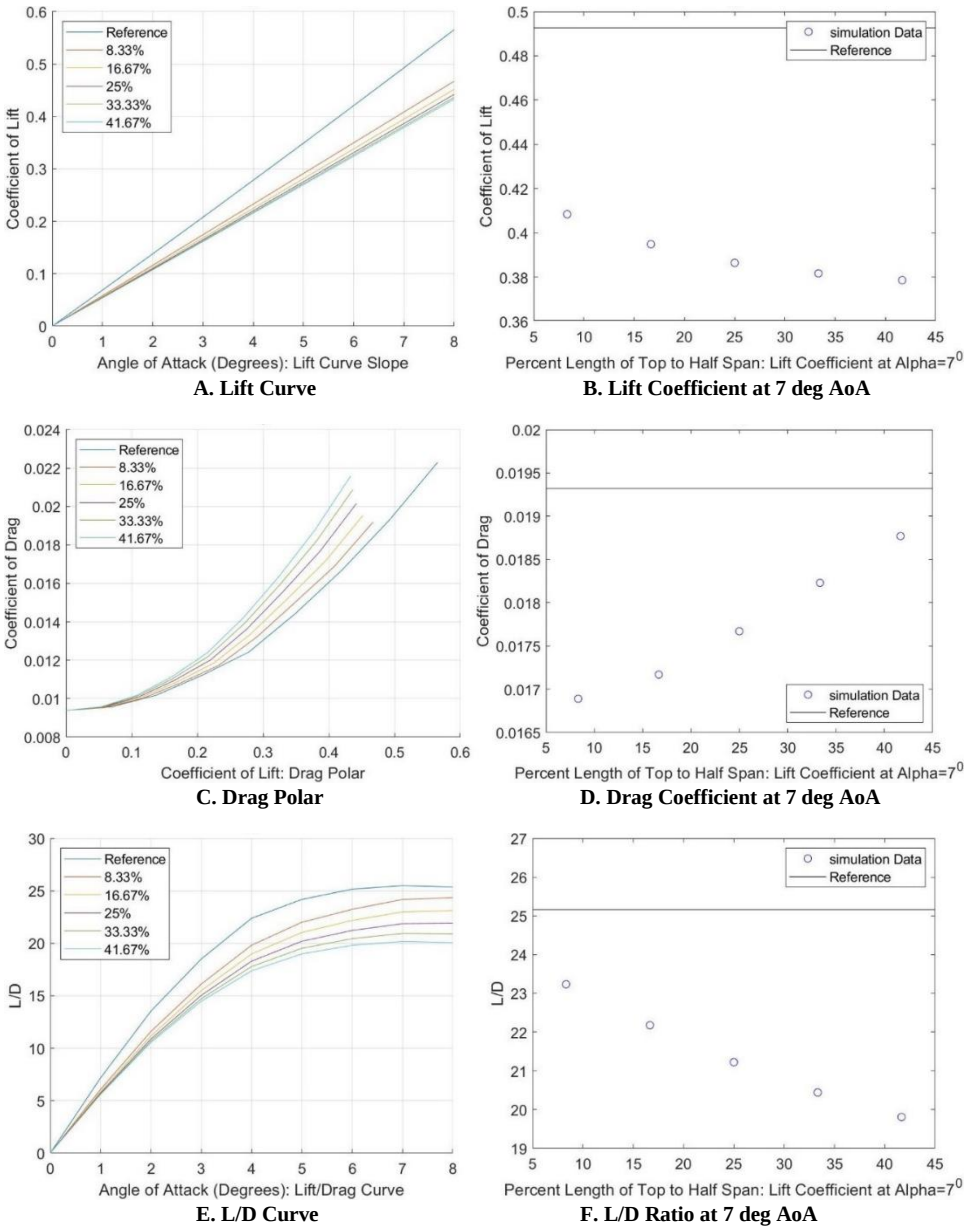

A. Lift Curve **B. Lift Coefficient at 7 deg AoA**

C. Drag Polar **D. Drag Coefficient at 7 deg AoA**

E. L/D Curve **F. L/D Ratio at 7 deg AoA**

Figure 20: C-wing Side 41.67%

Figure 20, sub-plots B and F show that the coefficient of lift and lift-to-drag ratio decreases linearly as the horizontal length increases. Sub-plot D shows the coefficient of drag increasing linearly as the horizontal length increases.

Figures 16-20, sub-plots A show that the lift curve slope decreases with respect to the reference as the vertical length increases for each horizontal length. Sub-plots B show that the coefficient of lift decreases

linearly as the horizontal length increases with the rate of decrease getting small as the vertical length increases. It is also observed that as the horizontal length increases, the maximum coefficient of lift decreases. Sub-plots C shows that the drag polar is larger compared to the reference for every wing except for the when the vertical length is 8.33% and the horizontal length is 8.33% and 16.67% respectively. Sub-plots D show that the coefficient of drag is relatively linear and starts to increase as the horizontal length increases. It is also observed that the minimum coefficient of drag decreases as the horizontal length increases and the minimum coefficient of drag is almost always located at a horizontal length of 8.33%. Sub-plot F shows that the lift-to-drag ratio decreases in a linear fashion as the horizontal section increases, and the maximum lift-to-drag ratio decreases as the vertical length is increases.

From Figures 16-20, it can be concluded that, in general the maximum lift coefficient and lift-to-drag ratio occur at horizontal length of 8.33% for all vertical lengths and decreases in a relatively linear fashion. It can also be concluded that the minimum coefficient of drag occurs at a horizontal length of 8.33% for all vertical lengths and increases in a relatively linear fashion.

3.1.2 Vertical C-wing Changes

For the vertical analysis of the C-wings, the focus of the analysis was in identifying trends for the coefficient of lift and drag and lift-to-drag ratios while the horizontal length was held constant. An angle of attack of seven degrees was chosen for a more in-depth analysis of each wing. The seven-degree angle of attack corresponds to the maximum lift-to-drag ratio for the reference wing. Figures 21-25 shows this analysis, where each figure is split into 6 sub-plots with each sub-plot being the same as the previous section.

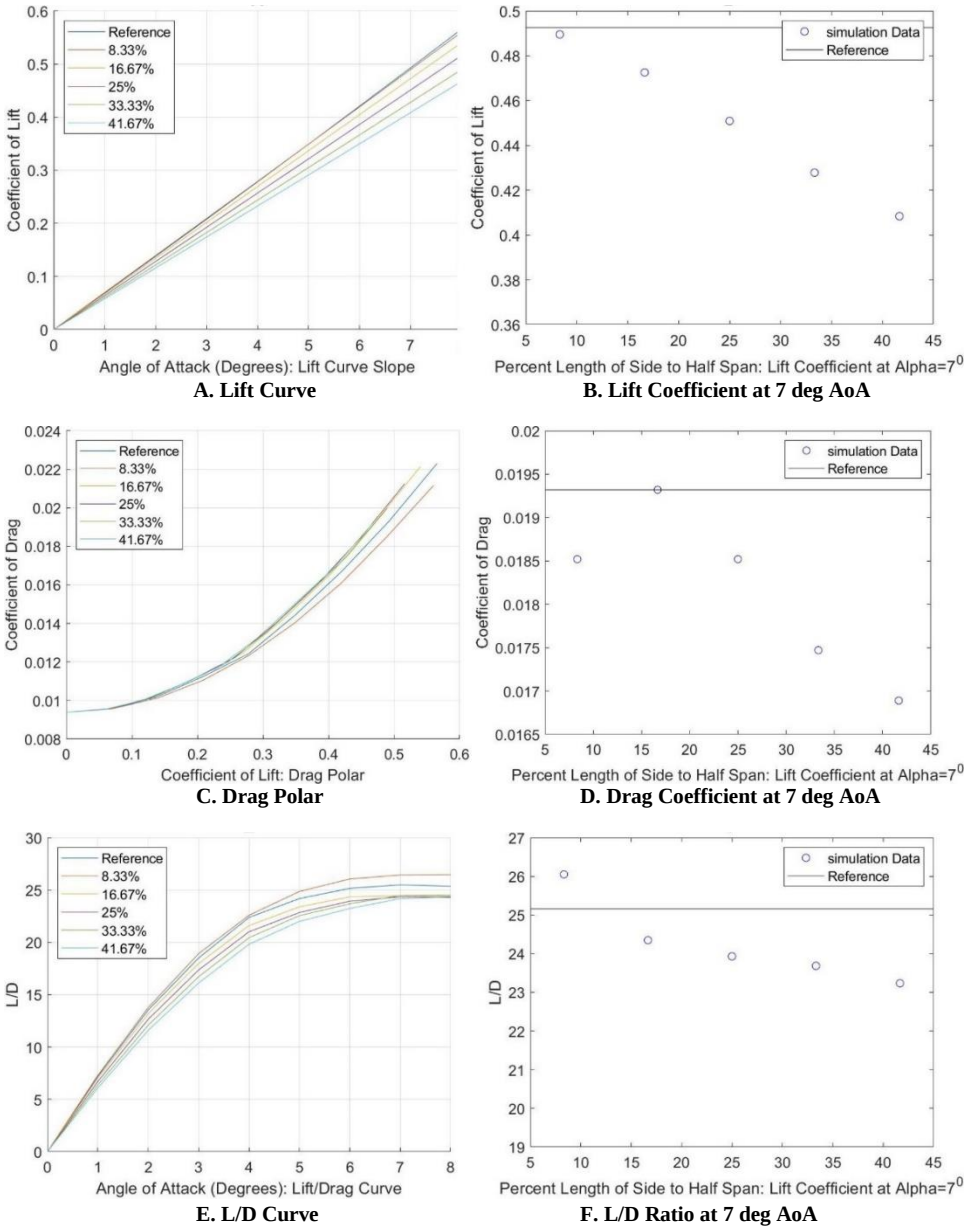

A. Lift Curve **B. Lift Coefficient at 7 deg AoA**

C. Drag Polar **D. Drag Coefficient at 7 deg AoA**

E. L/D Curve **F. L/D Ratio at 7 deg AoA**

Figure 21: C-wing Top 8.33%

Figures 21, sub-plot B shows that the coefficient of lift decreases linearly as the vertical length increases. Sub-plot D shows that the coefficient of drag increase from a vertical length of 8.33% to 16.67%, then decreases linearly after a vertical length of 16.67%. Sub-plot F shows that the lift-to-drag ratio decreases linearly as the vertical length increases. There was a larger decrease from a vertical length of 8.33% to 16.67% than at any other length change.

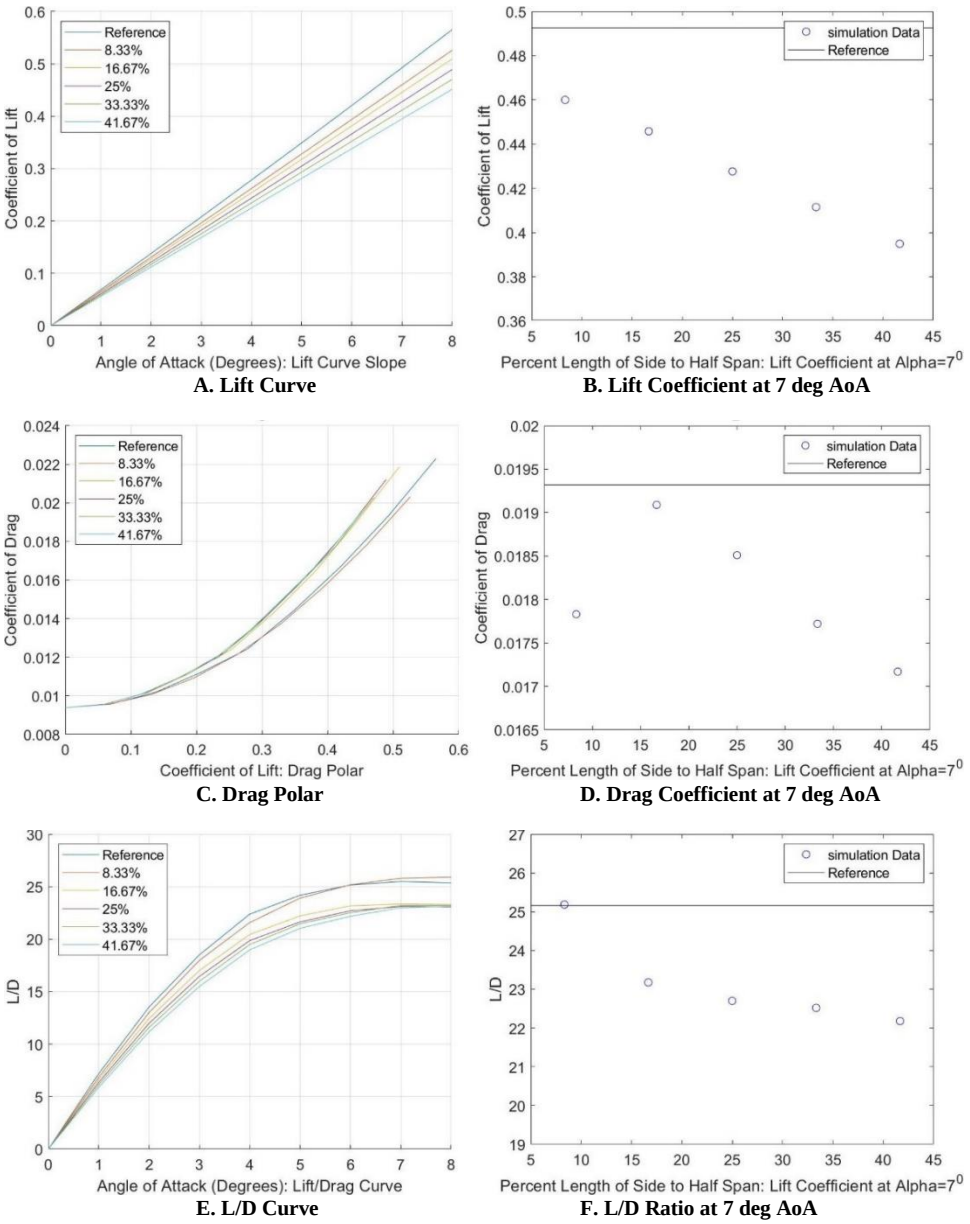

A. Lift Curve **B. Lift Coefficient at 7 deg AoA**

C. Drag Polar **D. Drag Coefficient at 7 deg AoA**

E. L/D Curve **F. L/D Ratio at 7 deg AoA**

Figure 22: C-wing Top 16.67%

Figures 22, sub-plot B shows that the coefficient of lift decreases linearly as the vertical length increases. Sub-plot D shows that the coefficient of drag increase from a vertical length of 8.33% to 16.67%, then decreases linearly after a vertical length of 16.67%. Sub-plot F shows that the lift-to-drag ratio decreases linearly as the vertical length increases. There was a larger decrease from a vertical length of 8.33% to 16.67% than at any other length change.

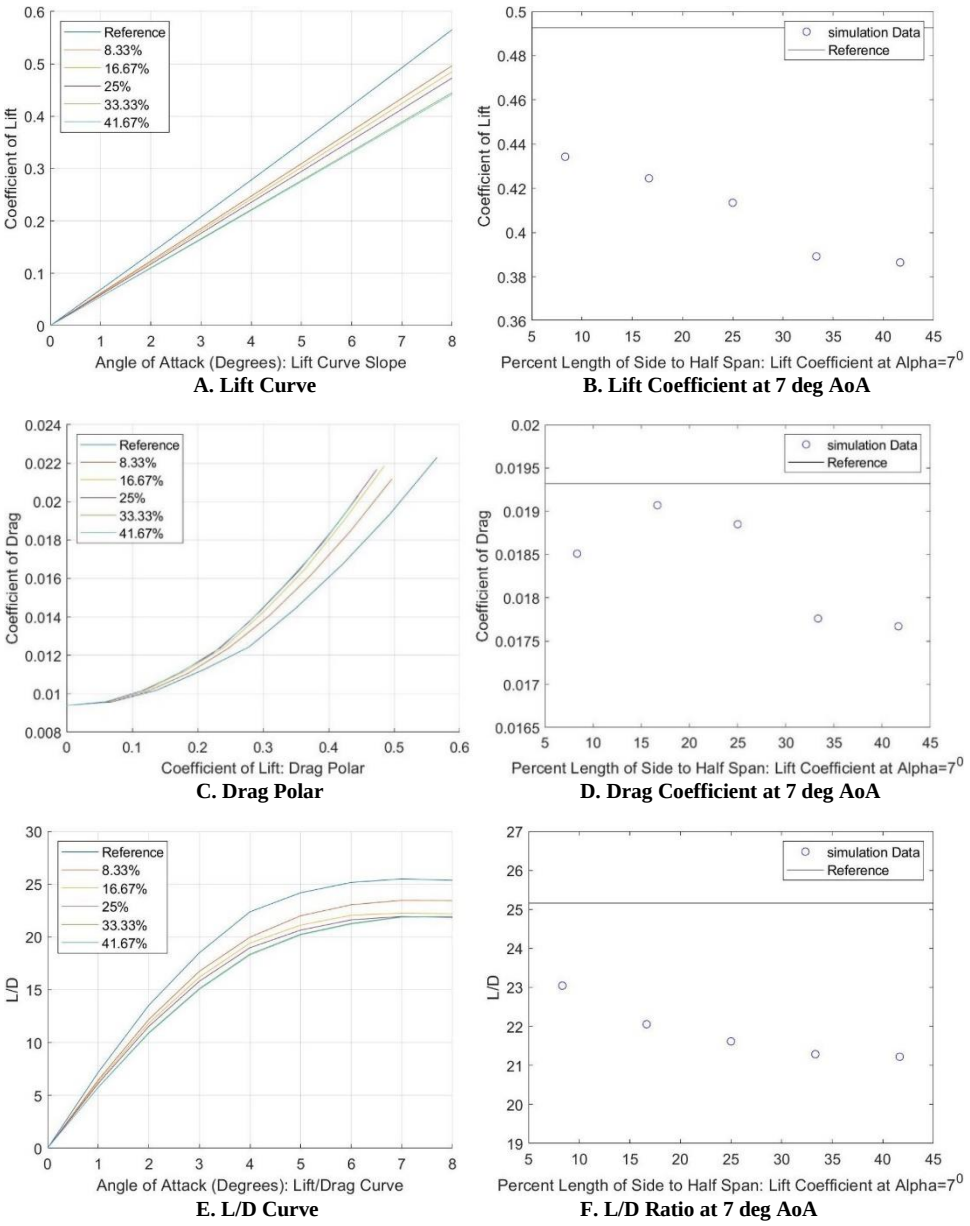

Figure 23: C-wing Top 25%

Figures 23, sub-plot B shows that the coefficient of lift decreases linearly as the vertical length increases except for when the vertical length is 33.33% and 41.67% where the coefficient of lift stays remains constant. Sub-plot D shows that the coefficient of drag increase from a vertical length of 8.33% to 16.67% then decreases after a vertical length of 16.67% to vertical length of 33.33%. After a vertical length of

33.33%, there is minimal change in the coefficient of drag. Sub-plot F shows that the lift-to-drag ratio decreases exponentially.

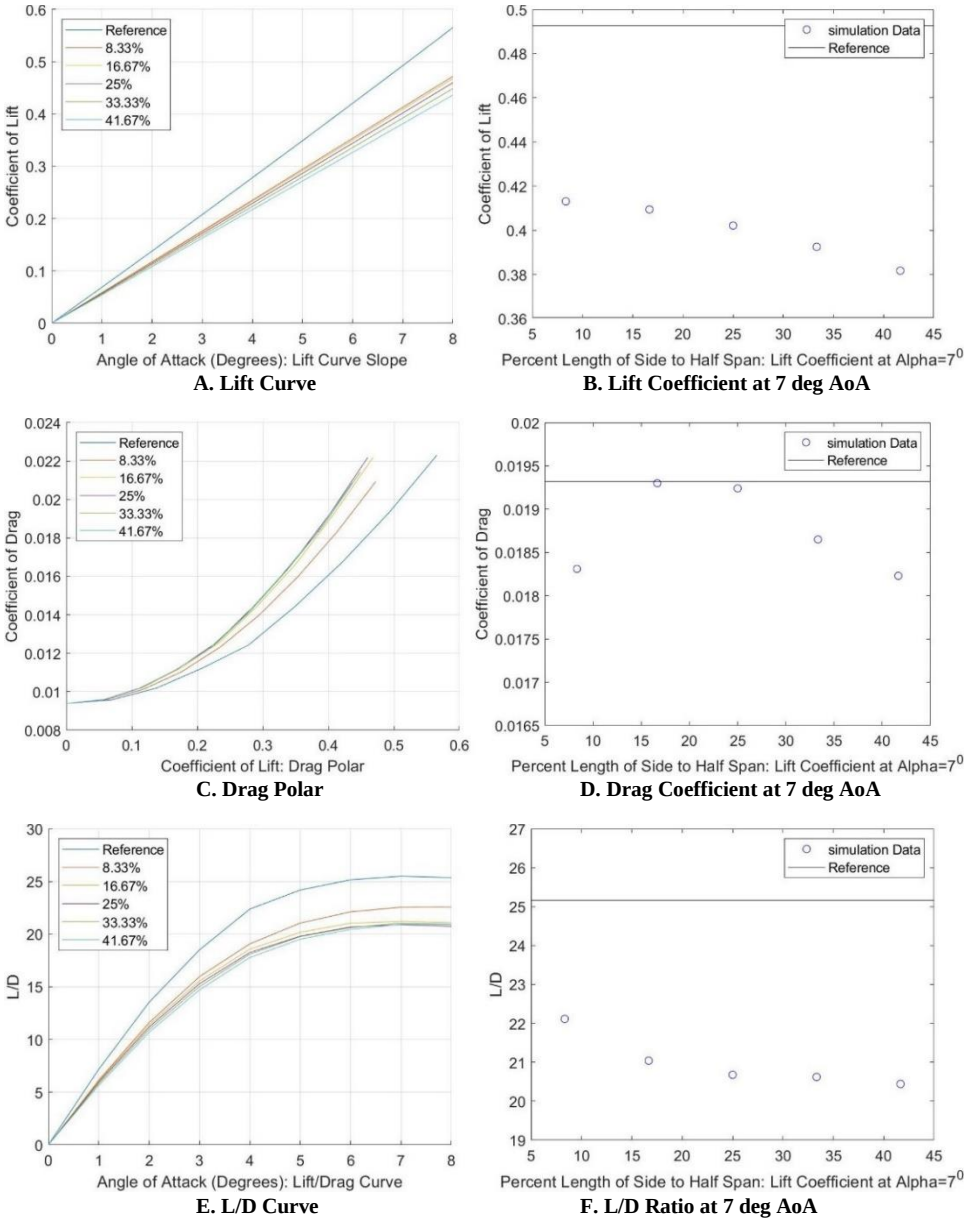

Figure 24: C-wing Top 33.33%

Figure 24, sub-plot B shows that the coefficient of lift decreases linearly as vertical length increases. Sub-plot D shows that the coefficient of drag increases from a vertical length of 8.33% to 16.67% then has

very little change from a vertical length of 16.67% to 25%. After a vertical length of 25%, the coefficient of lift decreases linearly. Sub-plot F shows that the lift-to-drag ratio decreases linearly from a vertical length of 8.33% to 25%.

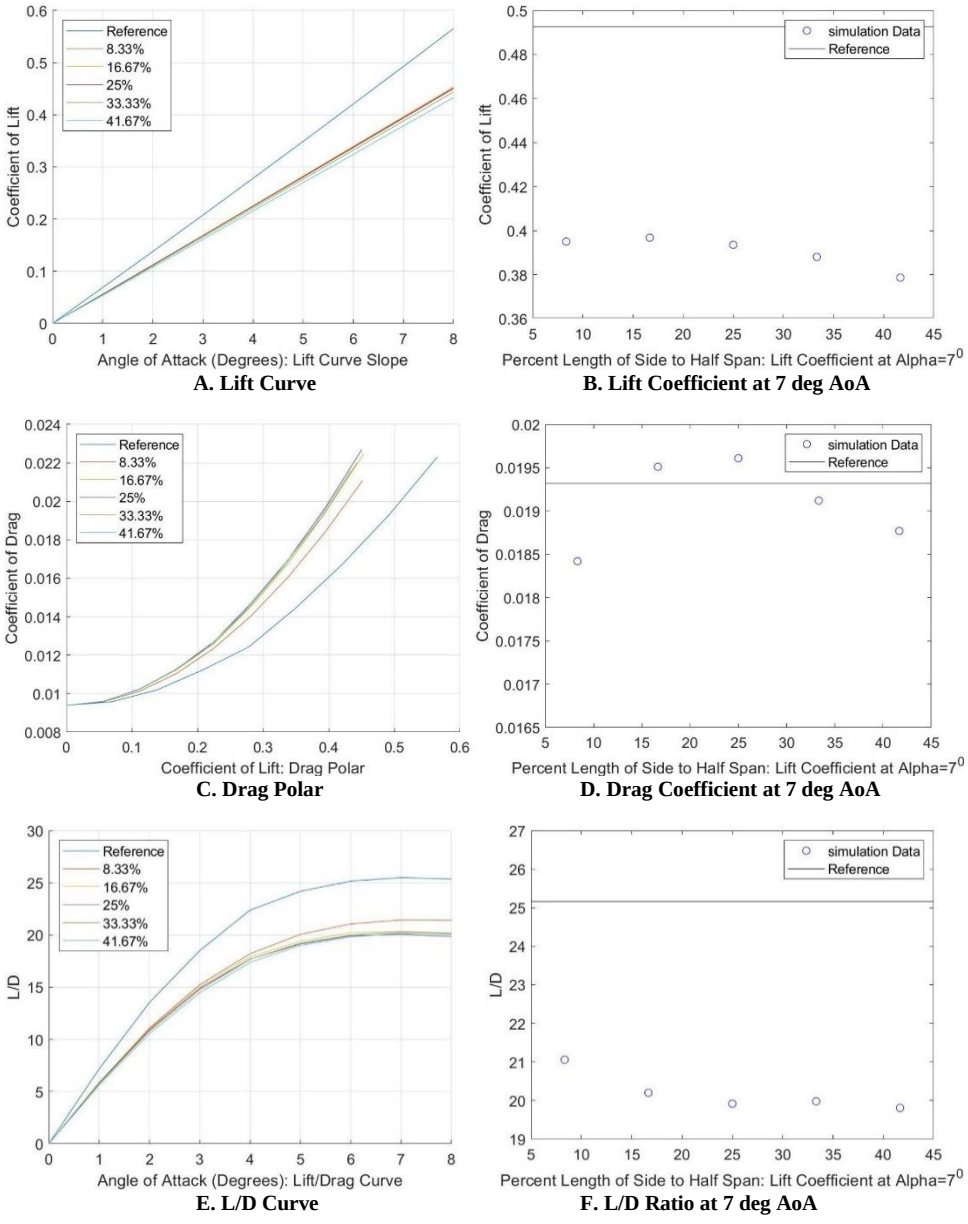

Figure 25: C-wing Top 41.67%

Figure 25, sub-plot B shows that the coefficient of lift stays about the same from a vertical length of 8.33% to 16.67% then decreases linearly as the vertical length increases. Sub-plot D shows that the coefficient of drag increases from a vertical length of 8.33% to 16.67% then increases slightly from vertical length 16.67% to 25%. After a vertical length of 25% it is observed that the coefficient of drag decreases linearly. Sub-plot F shows that lift-to-drag ratio decreases from a vertical length of 8.33% to 16.67%. After a vertical length of 16.67% the lift-to-drag ratio stays about the same until a vertical length of 41.67% where it decreases slightly.

Overall, Figures 21-25, sub-plots B shows that the coefficient of lift decreases linearly as the vertical section increases in length and that the maximum coefficient of lift decreases as the horizontal length increases. Sub-plot D shows that the initial coefficient of drag increases drastically after the vertical length increases above 8.33% then decreases linearly for the rest of the vertical length. It was also observed that the minimum coefficient of drag increases as the horizontal length increases. Sub-plot F shows that the maximum lift-to-drag ratio occurs at the shortest vertical length for all the horizontal lengths and decrease linear. Sub-plots F also show that as the maximum lift-to-drag ratio decreases as the horizontal length increases.

From Figures 21-25 it is determined that, in general, the maximum coefficient of lift and lift-to-drag ratio occurs at the shortest vertical length of 8.33% and decreases linearly as the vertical distance increases. It is also determined that the maximum coefficient of drag occurs at a vertical distance of 16.67% and decreases linearly as the vertical distance either increases or decreases.

3.2 Change in Vertical Section Sweep Angle of C-wing

This section will discuss how the aerodynamic performance of a C-wing changes as the sweep angle of the vertical section changes. The vertical sweep angle analyzed were the angles that caused the leading edge of the horizontal section of the C-wing to be from -100% to 100% behind of the leading edge of the main wing with respect to the chord. The analysis of the sweep angle was taken at 33.33% intervals. This can be seen below in Figure 26, when the leading edge of each wing is on the left, and with wing A being at -100%

and wing G being at 100%. Figures 27-35 show this analysis, where each figure is split into 6 sub-plots, with each sub-plot being the same as section 3.1.1.

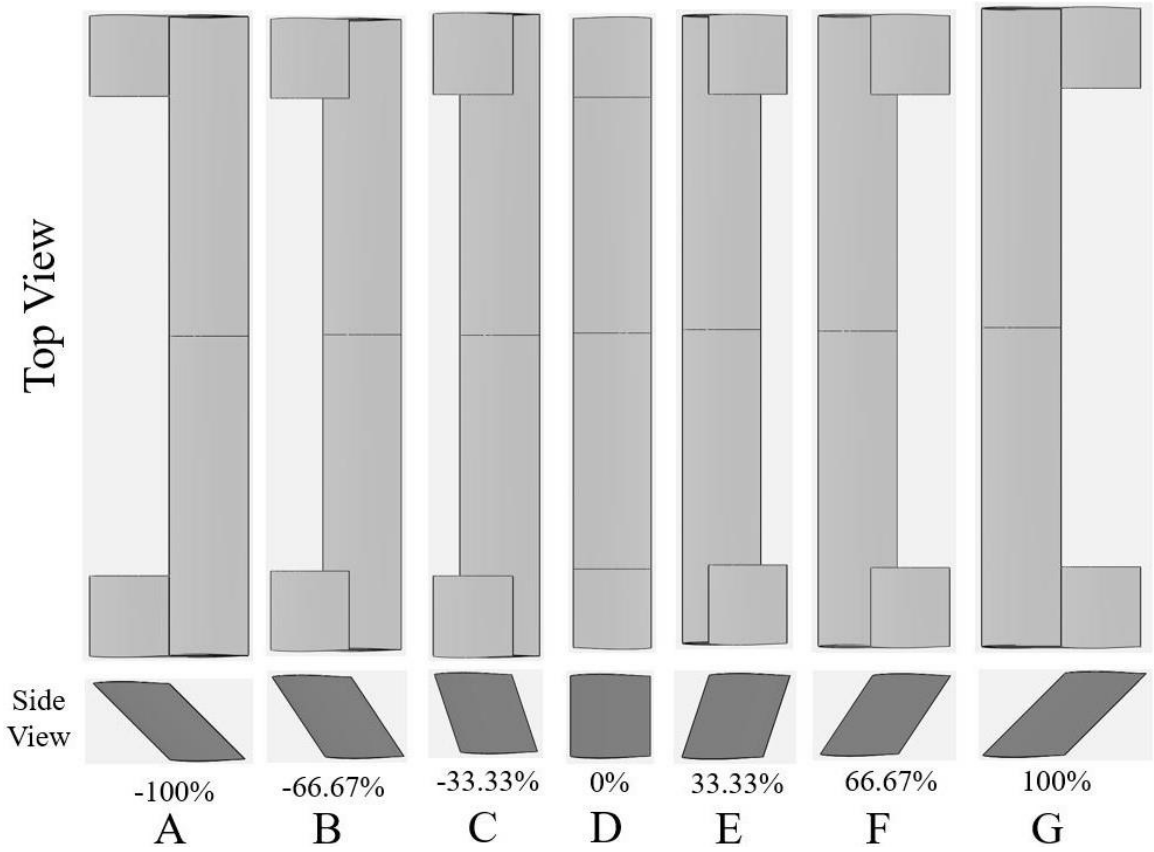

Figure 26: Sweep angles

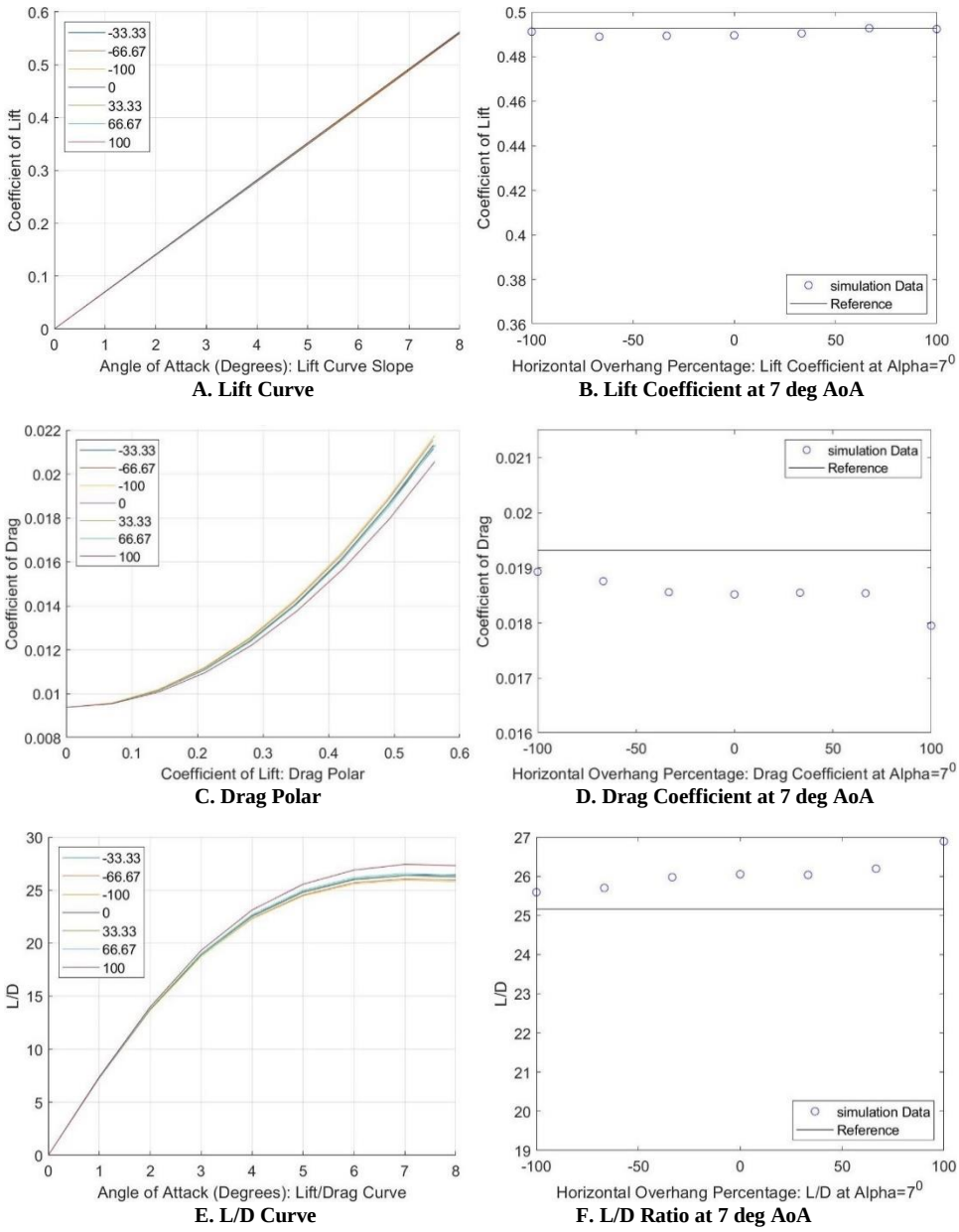

Figure 27: C-wing Side 8.33% Top 8.33%

Figure 27, sub-plot B shows that the coefficient of lift increases slightly as the sweep angle increases. Sub-plot D shows that the coefficient of drag slightly decreases between sweep angles of -100% to -66.67% and from 66.67% to 100%. It is also observed that the coefficient of drag does not change between the sweep angles of -33.33% and 66.67%. Sub-plot F shows that the lift-to-drag ratio increase as sweep angle increases except between the angles of -33.33% and 33.33% where it remains the same.

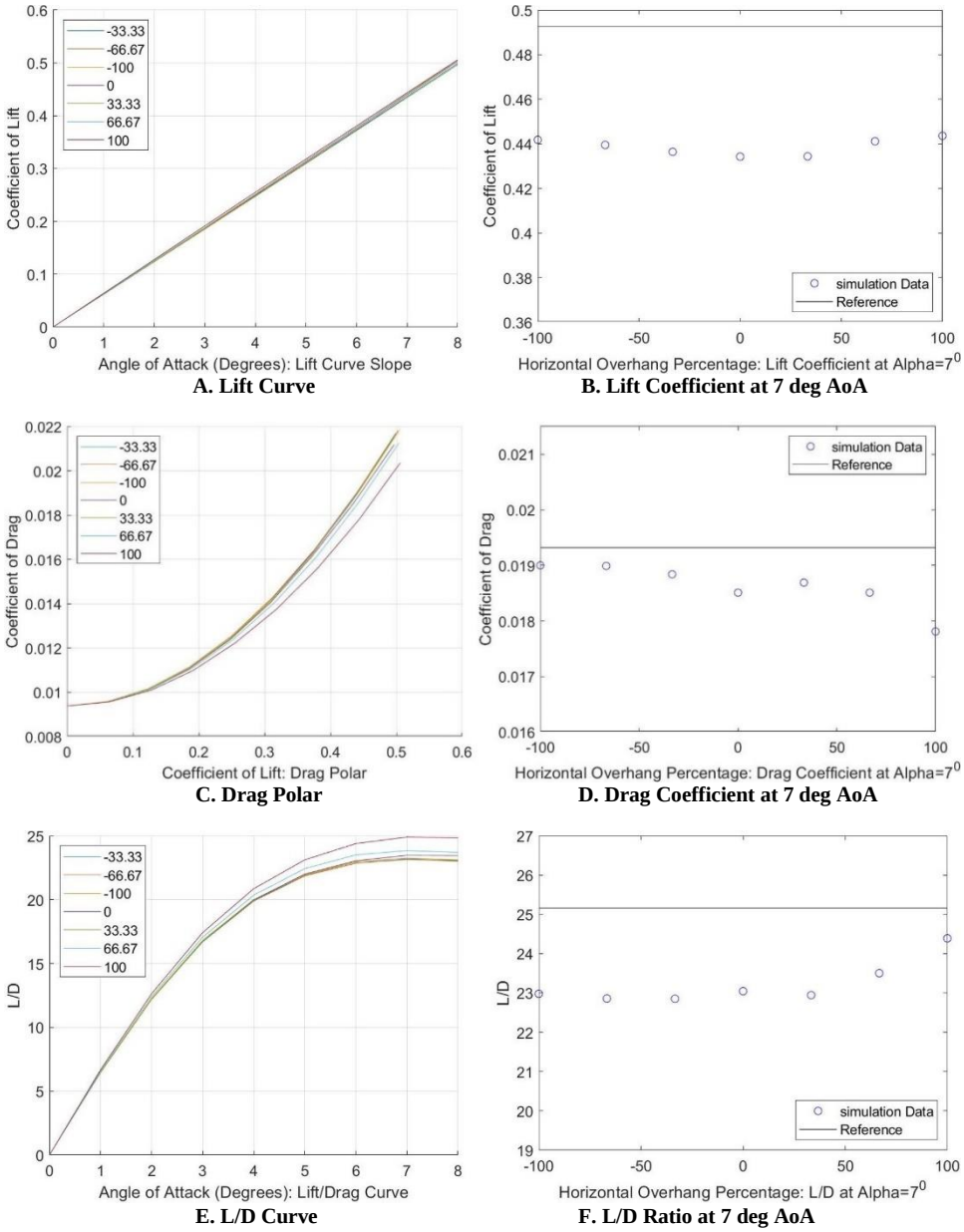

Figure 28: C-wing Side 8.33% Top 25%

Figure 28, sub-plot B shows that the coefficient of lift stays about the same as the sweep angle increases with a slight dip around a sweep angle of 0%. Sub-plot D shows that the coefficient of drag decreases linearly as the sweep angle increases, except between sweep angles of 0% and 33.33% where the coefficient of drag increases slightly. Sub-plot F shows that the lift-to-drag ratio stays constant from a sweep angle of -100% to 33.33% after which it increases linearly.

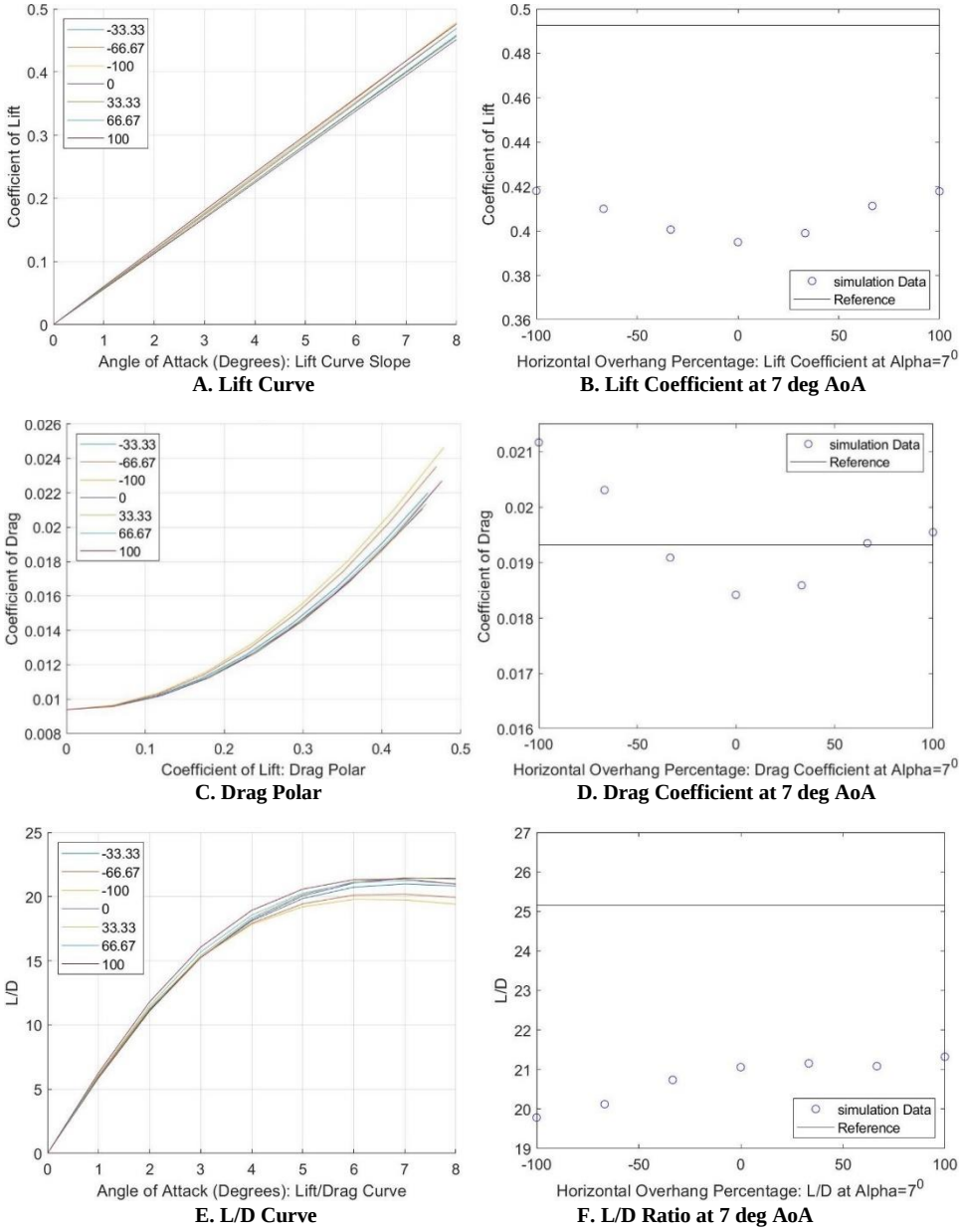

Figure 29: C-wing Side 8.33% Top 41.67%

Figure 29, sub-plot B shows that the coefficient of lift makes a parabolic shape and decreases between a sweep angles of -100% to 0% and increases from 0% to 100%. Sub-plot D shows that the coefficient of drag makes a parabolic shape and decreases from a sweep angle of -100% to 0% and increases from 0% to 66.67%. From a sweep angle of 66.67% to 100% the coefficient increases slightly but does not

follow a parabolic shape. Sub-plot F shows that the lift-to-drag ratio increase linearly as the sweep angle increases except between the sweep angles of 0% and 66.67% where it remains constant.

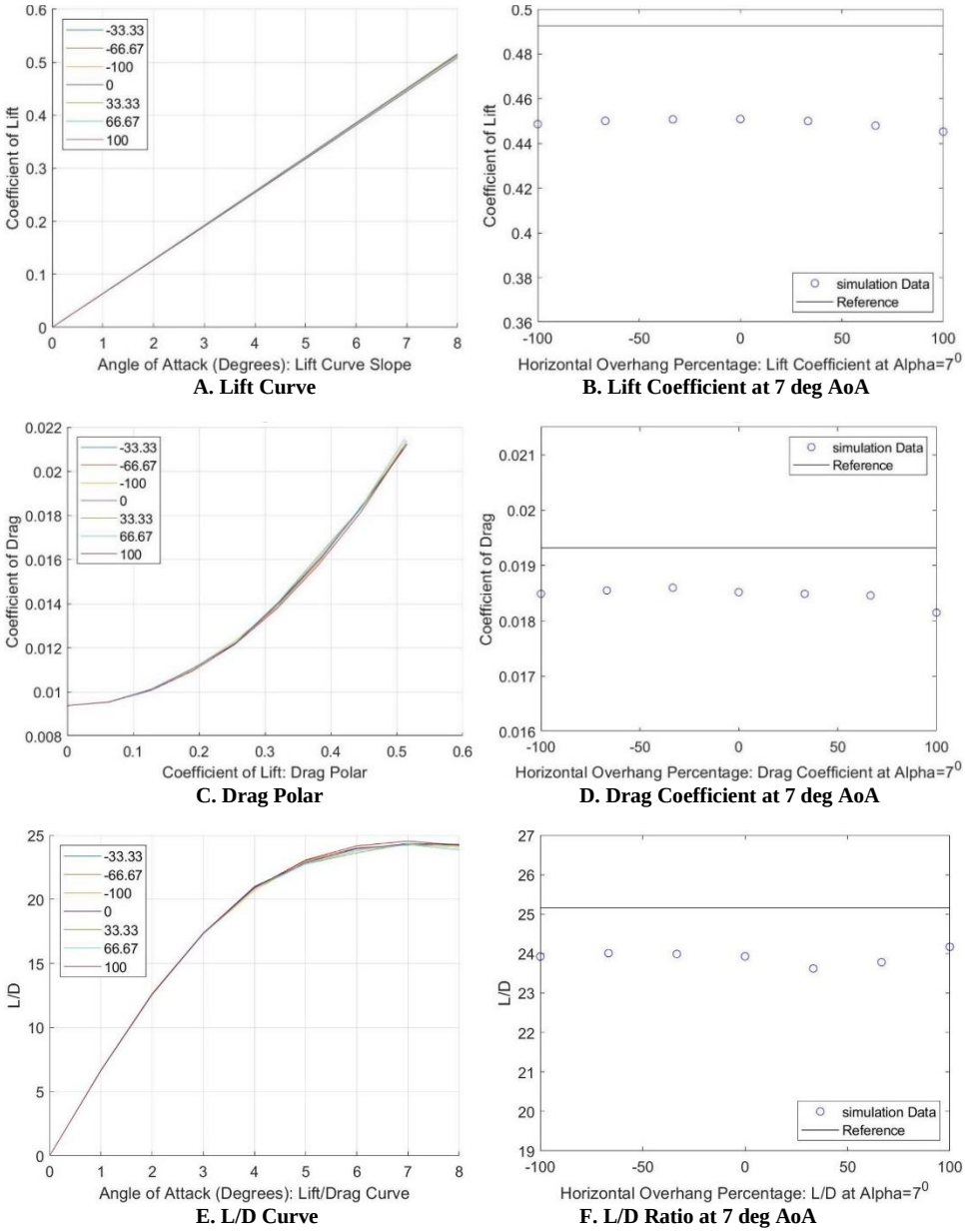

Figure 30: C-wing Side 25% Top 8.33%

Figure 30, sub-plot B shows that the coefficient of lift stays relatively constant and only decreases slightly as the sweep angle increases. Sub-plot D shows that the coefficient of drag stays the same as the

sweep angle increases except at a sweep angle of 100% where it decreases slightly. Sub-plot F shows that the lift-to-drag ratio increases linearly between sweep angles -100% and 0%. After a sweep angle 0%, the lift-to-drag ratio decreases slightly then increases linearly.

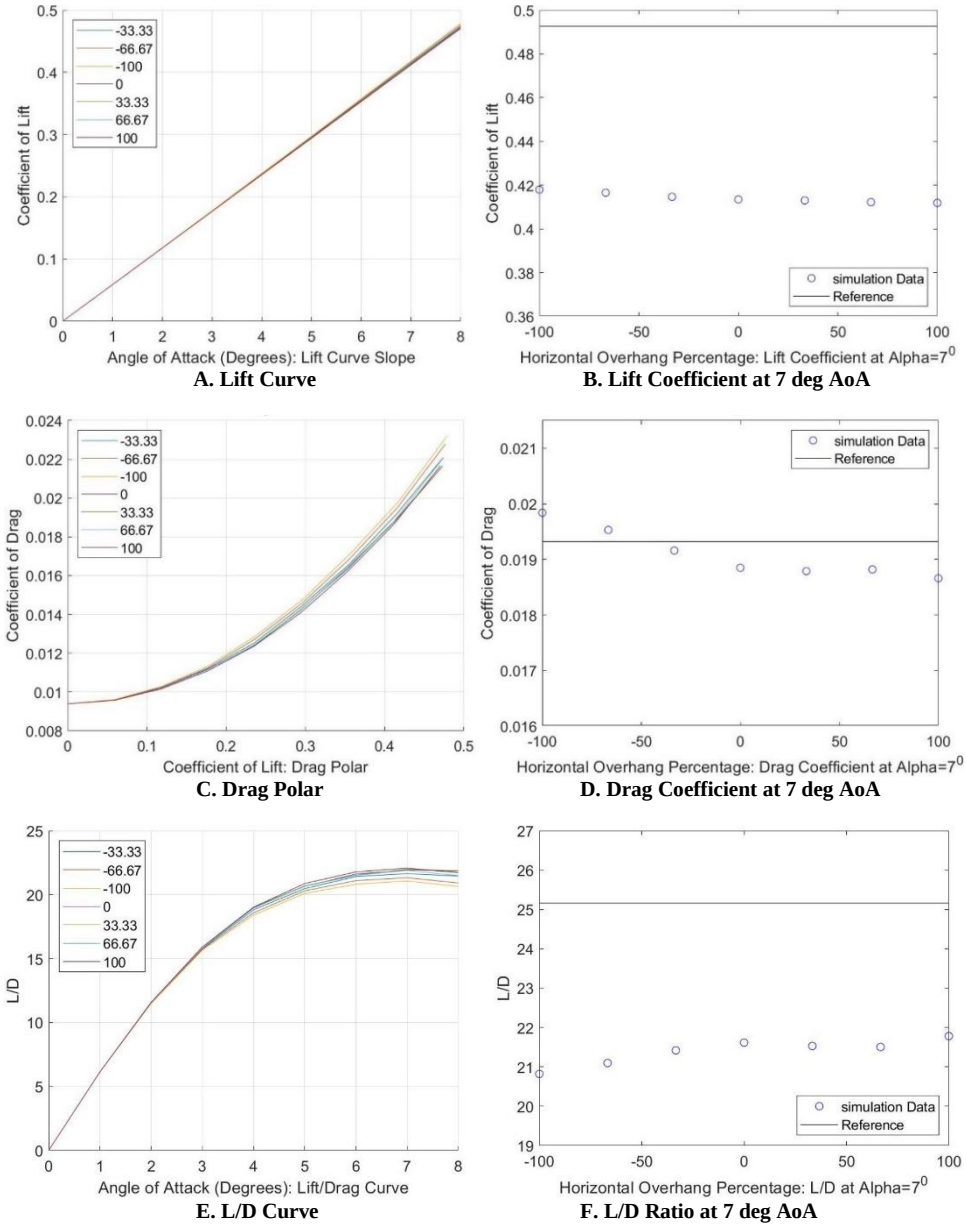

Figure 31: C-wing Side 25% Top 25%

Figure 31, sub-plot B shows that the coefficient of lift decreases slightly as sweep angle is increased. Sub-plot D shows that the coefficient of drag decreases linearly as the sweep angle increases, except between sweep angles of 0% and 66.67% where the coefficient of drag remains constant. Sub-plot F shows that the lift-to-drag ratio increases linearly as the sweep angle increases except between the sweep angles of 0% and 66.67% where it remains constant.

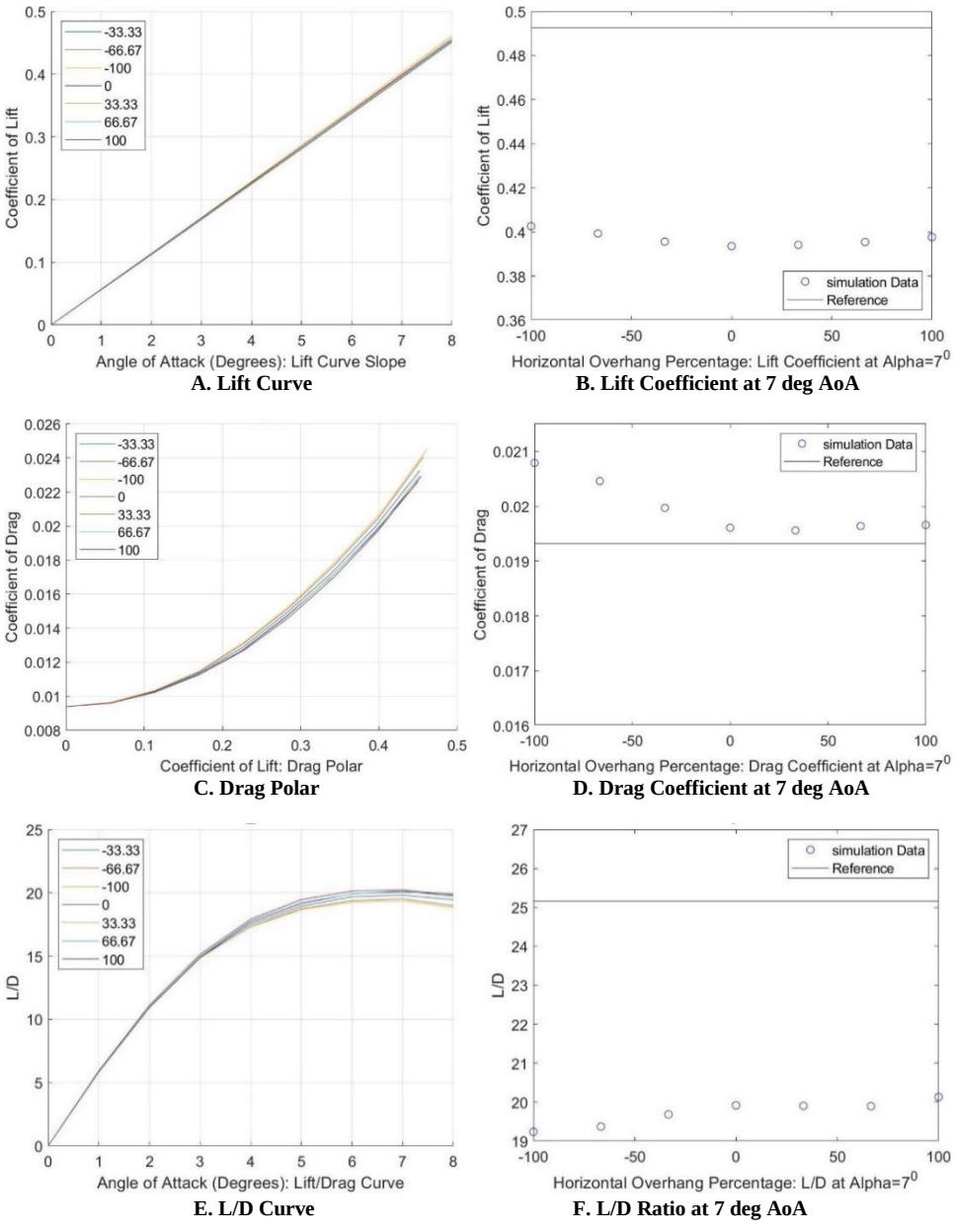

A. Lift Curve **B. Lift Coefficient at 7 deg AoA**

C. Drag Polar **D. Drag Coefficient at 7 deg AoA**

E. L/D Curve **F. L/D Ratio at 7 deg AoA**

Figure 32: C-wing Side 25% Top 41.67%

Figure 32, sub-plot B shows that the coefficient of lift decreases slightly as the sweep angle increases. Sub-plot D shows that the coefficient of drag decreases linearly between sweep angles of -100% and 0%, after a sweep angle of 0% the coefficient of drag increases slightly. Sub-plot F shows that the lift-to-drag ratio increases linearly as the sweep angle increases except between the sweep angles of 0% and 66.67% where it remains constant.

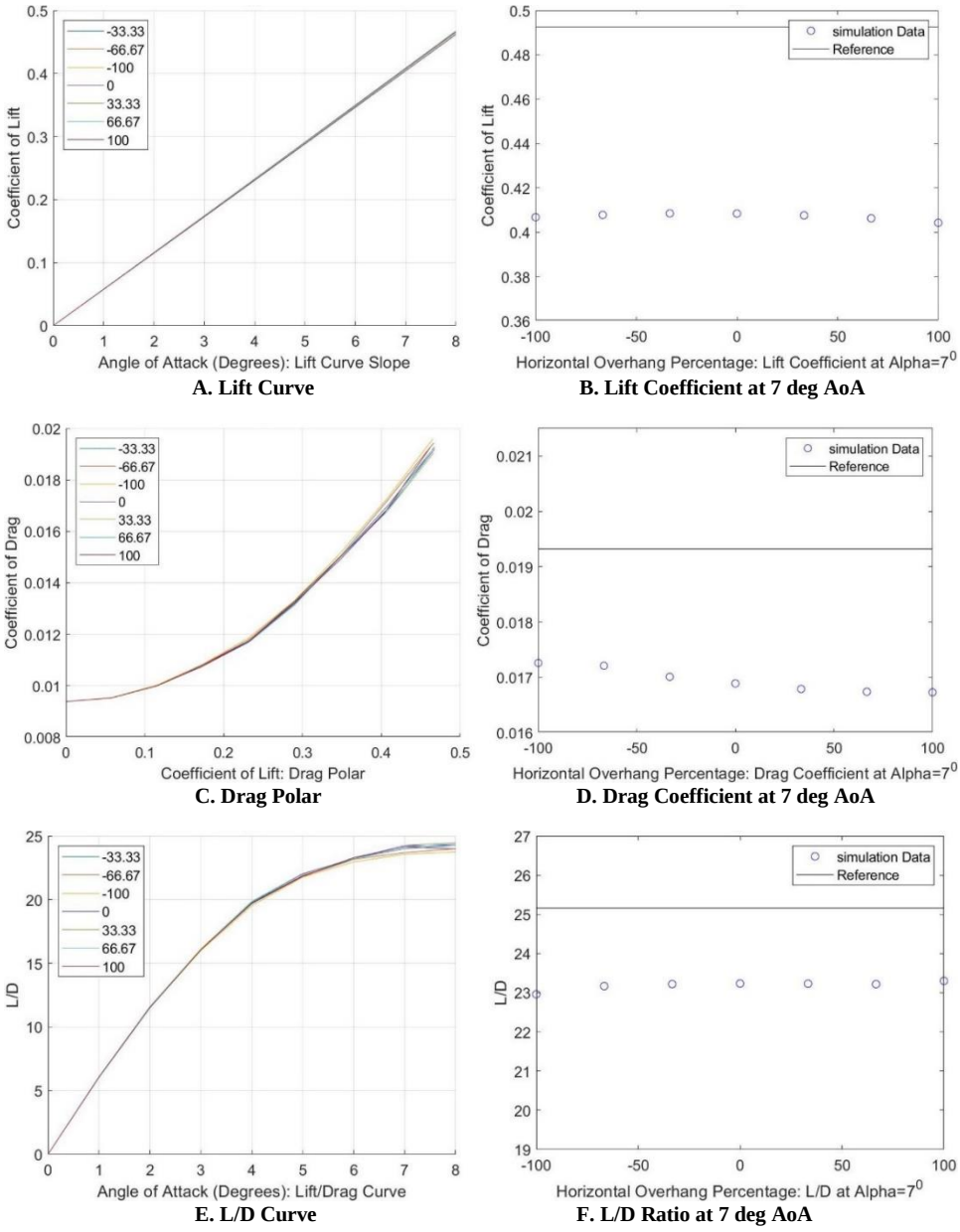

A. Lift Curve **B. Lift Coefficient at 7 deg AoA**

C. Drag Polar **D. Drag Coefficient at 7 deg AoA**

E. L/D Curve **F. L/D Ratio at 7 deg AoA**

Figure 33: C-wing Side 41.67% Top 8.33%

Figure 33, sub-plot B shows that the coefficient of lift remains constant as the sweep angle increases. Sub-plot D shows that the coefficient of drag decreases linearly between sweep angles of -100% and 0%, after a sweep angle of 0% the coefficient of drag remains the same. Sub-plot F shows that the lift-to-drag ratio increases slightly as the sweep angle increases.

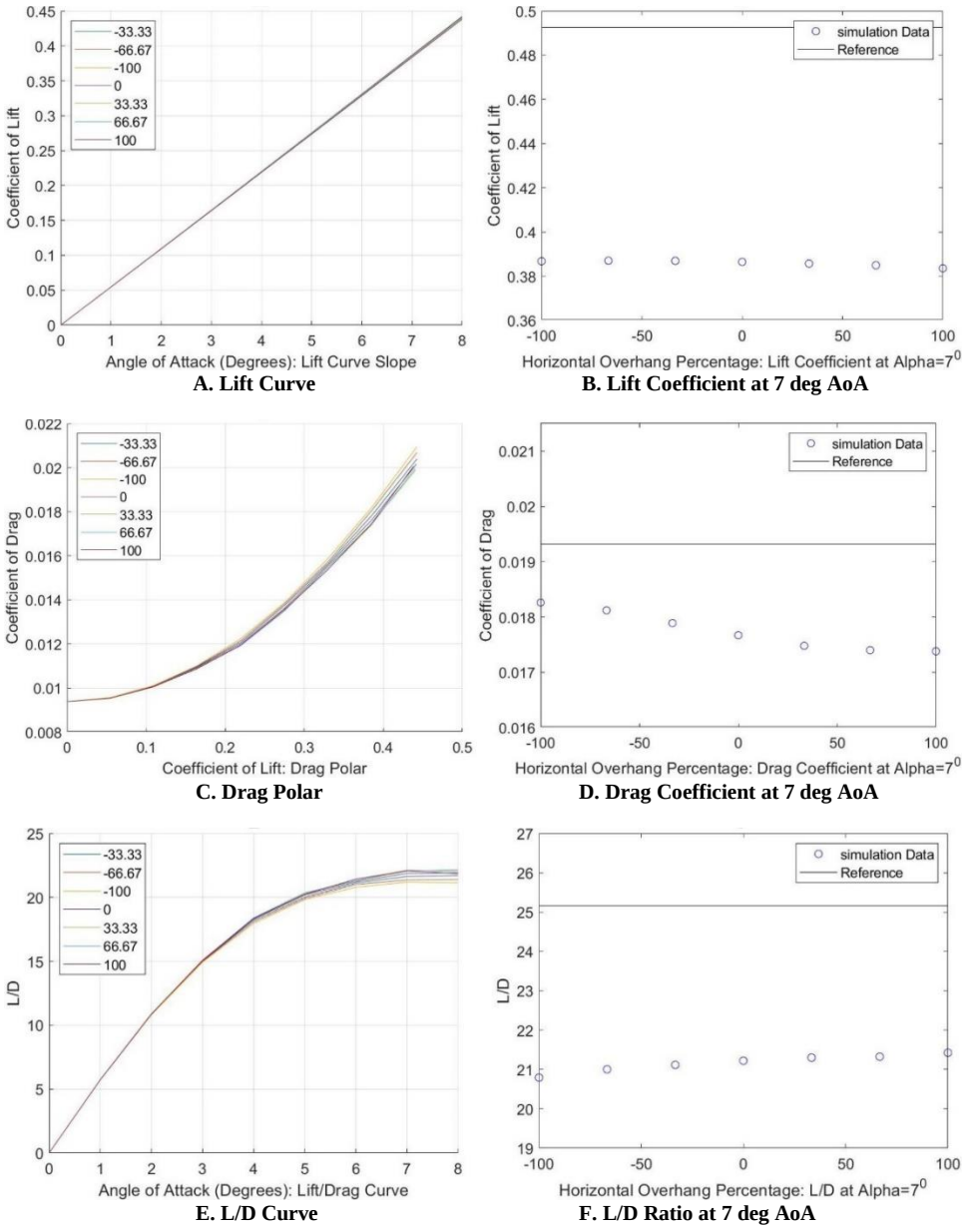

A. Lift Curve **B. Lift Coefficient at 7 deg AoA**

C. Drag Polar **D. Drag Coefficient at 7 deg AoA**

E. L/D Curve **F. L/D Ratio at 7 deg AoA**

Figure 34: C-wing Side 41.67% Top 25%

Figure 34, sub-plot B shows that the coefficient of lift remains constant as the sweep angle increases. Sub-plot D shows that the coefficient of drag decreases linearly between sweep angles of -100% and 33.33%, after a sweep angle of 33.33% the coefficient of drag remains the same. Sub-plot F shows that the lift-to-drag ratio increases linearly as the sweep angle increases.

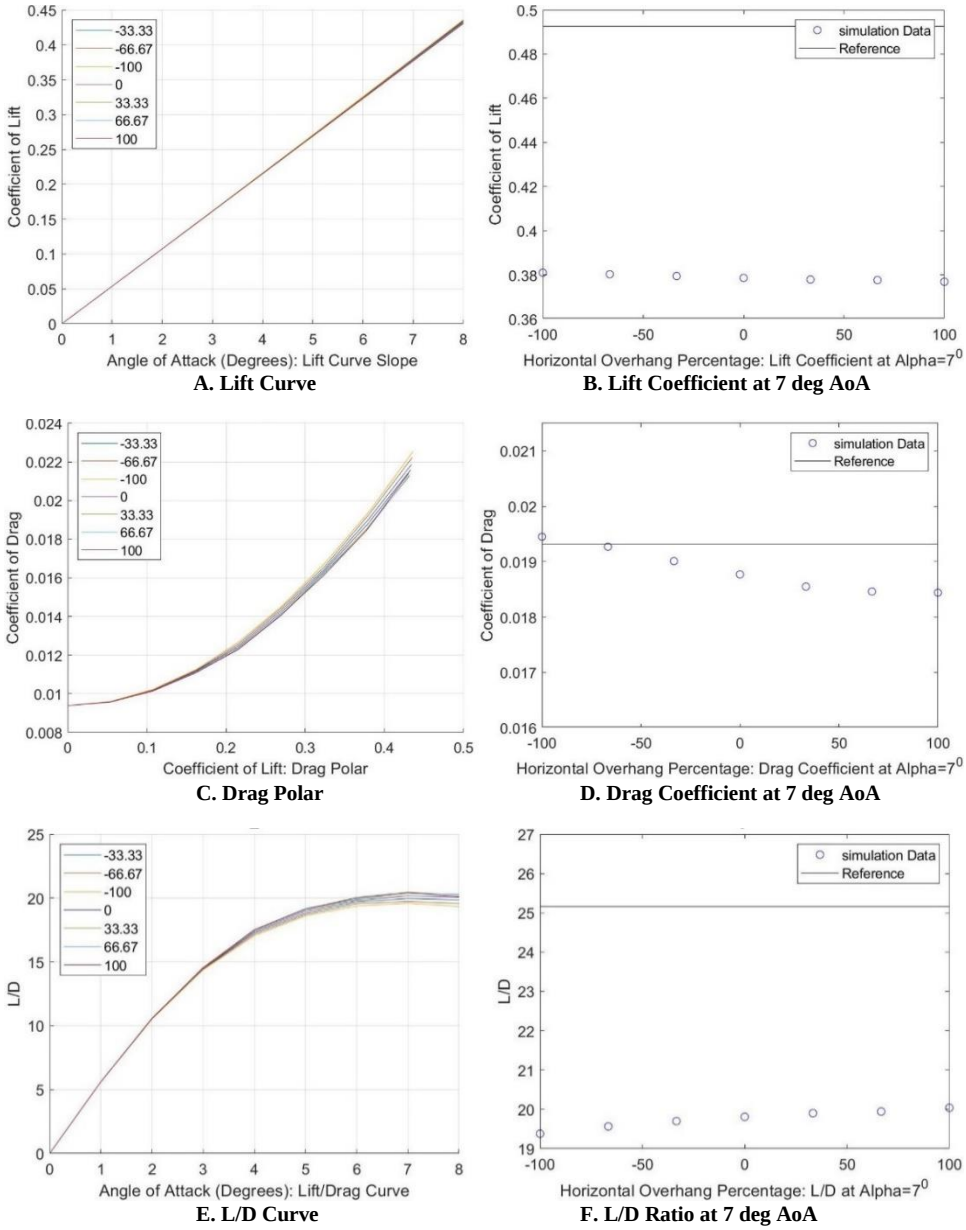

Figure 35: C-wing Side 41.67% Top 41.67%

Figure 35, sub-plot B it is observed that the coefficient of lift remains the same as the sweep angle increases. Sub-plot D shows that the coefficient of drag decreases linearly between sweep angles of -100% and 33.33%, after a sweep angle of 33.33% the coefficient of drag remains the same. Sub-plot F shows that the lift-to-drag ratio increases linearly as the sweep angle increases.

Overall, Figures 27-35, sub-plots A show that the lift curve slope changes between 1%-5% when the sweep angle changes. Sub-plots B show the coefficient of lift increases then decrease linearly as the sweep angle increases when either the vertical length is greater than 8.33% or the horizontal length is greater than 41.67%. This holds true except for when the vertical length is 8.33% and the horizontal length is 41.67% when, the coefficient of lift makes a parabolic shape. Sub-plots C shows that the lowest drag polar occurs when the sweep angle is 100% for every C-wing. Sub-plots D show that the coefficient of drag tends to decrease relatively linearly as the sweep angle increases. This holds true except for when the vertical length is 8.33% and the horizontal length is 41.67% when the coefficient of drag makes a parabolic shape. Sub-plots E show that a sweep angle of 100% gives the largest lift-to-drag plot. Sub-plots F show lift-to-drag ratio tends to increase linearly as the sweep angle increase.

Figures 27-35 also show that changing the sweep angle dynamically in flight could offer away to control an aircraft. This could be done by increasing or decreasing the sweep angle, this would moving the top of the C-wing forward and backwards and have very little affect on the aerodynamic performance. This would cause the aerodynamic center to move forward and backwards inducing a pitching moment on the aircraft. Also increasing the sweep angle on one wing and decreasing the sweep angle on the other wing would move the aerodynamic center left and right inducing a yaw/rolling moment on the aircraft.

From Figures 27-35, it is observed that, the coefficient of lift either increases or decreases linearly as the sweep angle increases, depending on the size of the C-wing. The coefficient of drag decreases linearly as the sweep angle increases, and the lift-to-drag ratio increases linearly as the sweep angle increases. Finally, changing the sweep angle dynamically in flight could be used to control the aircraft.

Chapter 4. Parametric Study

This chapter will discuss the trends of varying C-wing geometric parameters. Contour plots are provided below. Figure 36 shows the coefficient of lift, Figure 37 shows coefficient of drag, and Figure 38 shows the lift-to-drag ratio. The change in the horizontal length of the C-wing is plotted on the x-axis and the change in the vertical length is plotted on the y-axis.

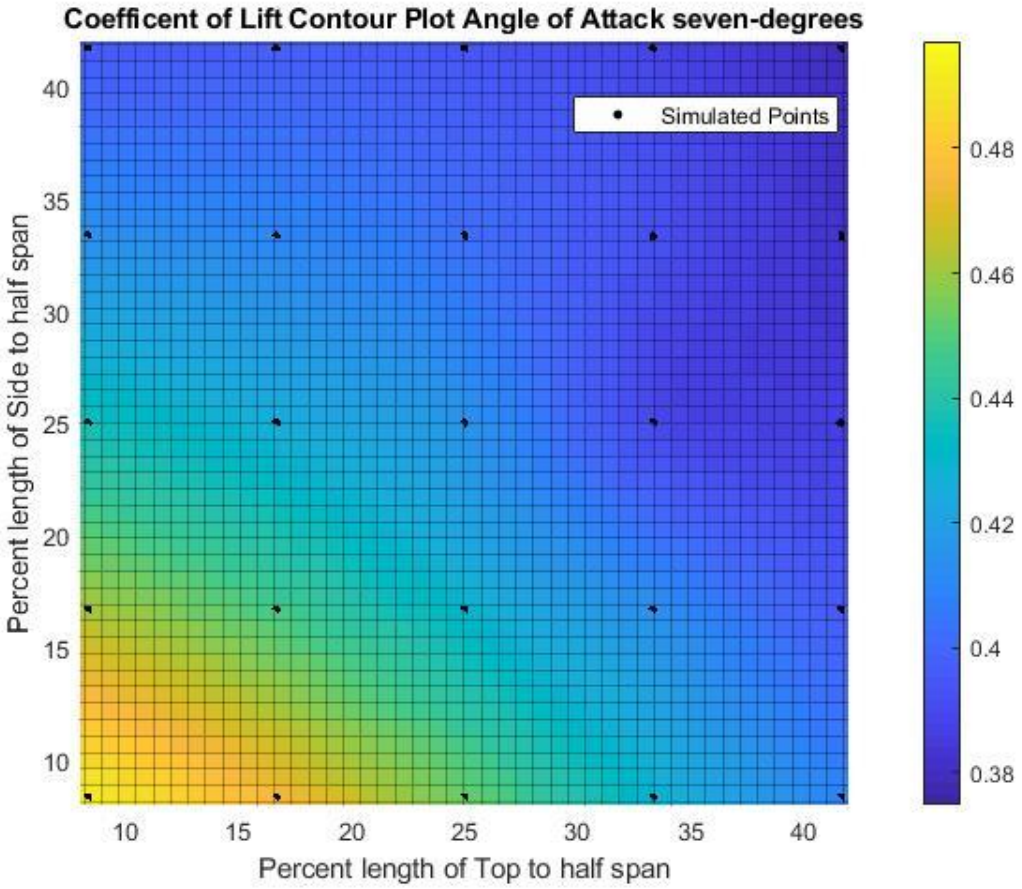

Figure 36: Coefficient of Lift Contour Plot

Figure 36 shows that a local maximum occurs in the bottom left hand corner of the graph where both the vertical and horizontal distance are less than 12%. It is also observed that a local minimum occurs at the top right corner where both the vertical and horizontal lengths are greater than 37%. It can be seen that the coefficient of lift decreases as the vertical and horizontal section lengths increases, individually and simultaneously.

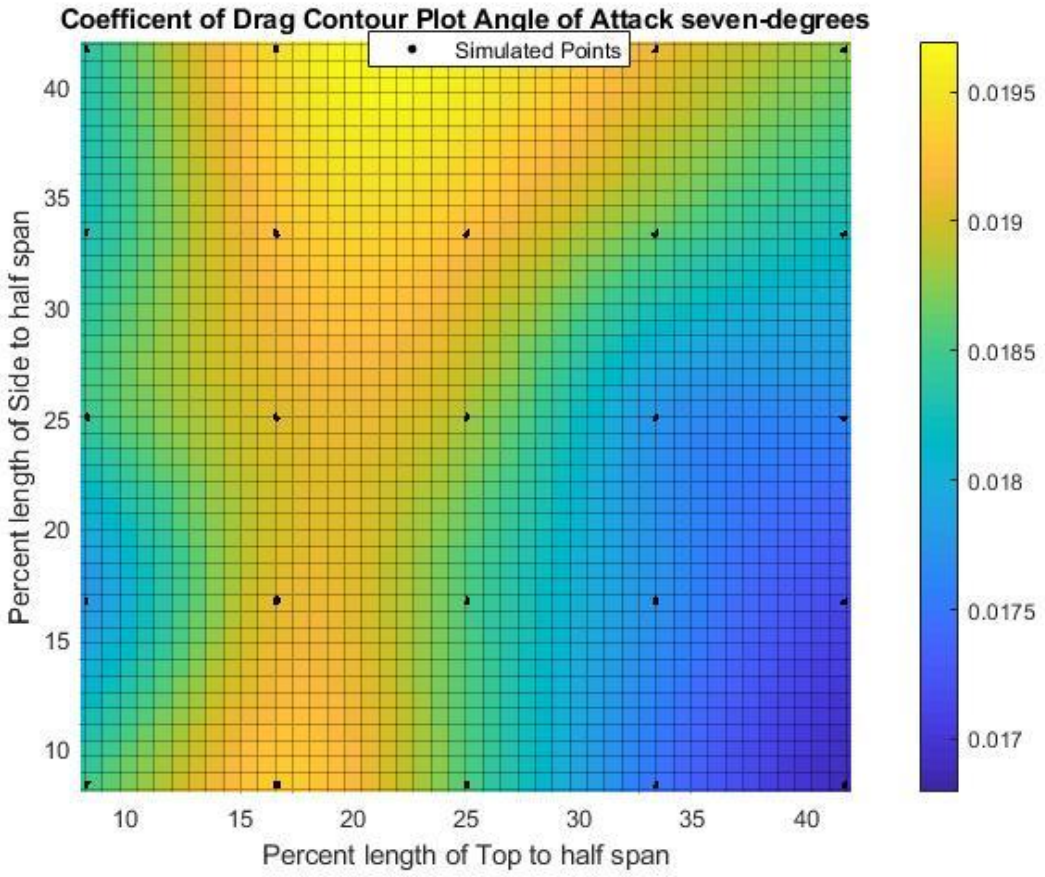

Figure 37: Coefficient of Drag Contour Plot

Figure 37 shows that there are definable regions of high and low coefficients of drag for the C-wing geometric configurations investigated. A high peak in drag occurs between horizontal lengths of 15% to 20% when the vertical length is less than 10%. A second, more localized, peak occurs at a horizontal length

between 18% to 25%, and when the vertical length is greater than 37%. Two valleys in drag are observed. The first local valley occurs between vertical lengths of 15% to 20% and when the horizontal length is less than 10%. The second local valley occurs at the bottom right hand corner when the horizontal length is greater than 37% and the vertical length is less than 12%.

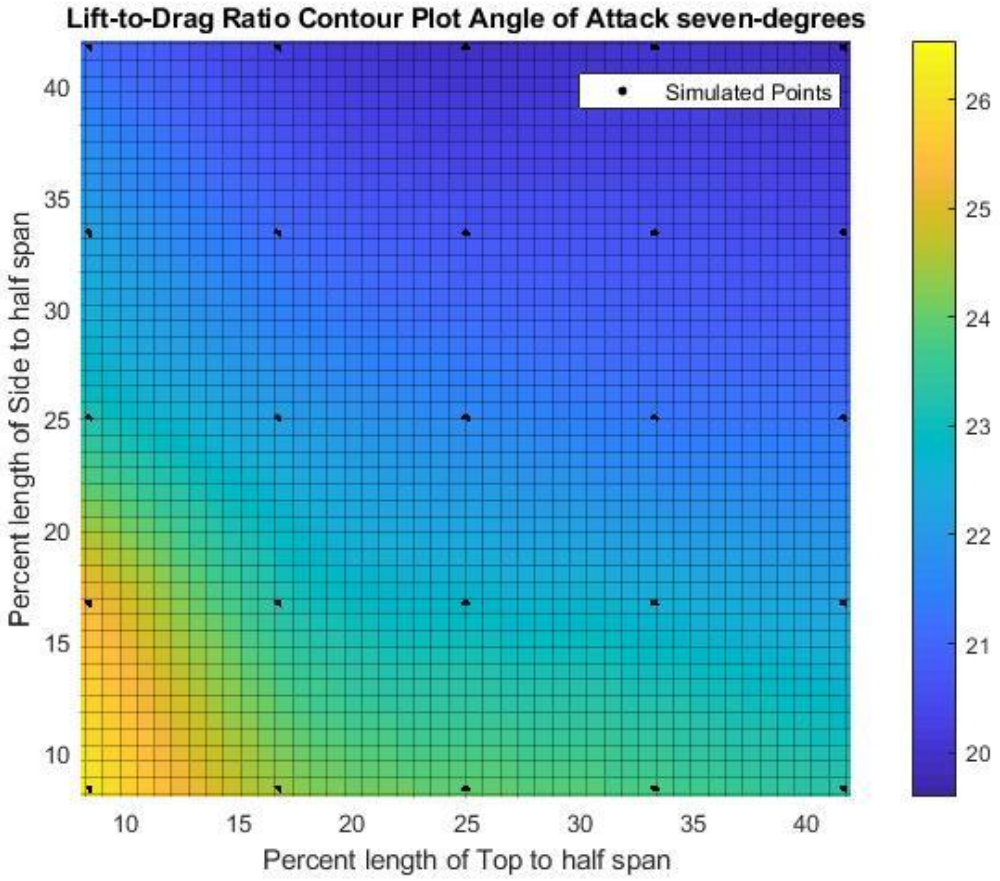

Figure 38: Lift-to-Drag Ratio Contour Plot

Figure 38 shows that the lift-to-drag ratio has a local peak near the shortest C-wing configurations investigated. This occurs when the vertical length is less than 15% and the horizontal length is less than 10%. It is also observed that the lift-to-drag ratio decreases as the vertical and horizontal section lengths increase

simultaneously. It is also observed that when the horizontal length is greater than 20%, for the shortest vertical length, the lift-to-drag ratio is held constant with further increase in the horizontal length.

From Figures 36-37, it can be determined that there is a local maximum point when the vertical length is between 12-17% and the horizontal length is less than 12%. In this area, the coefficient of drag has a local minimum point, and the coefficient of lift and lift-to-drag ratio have locally maximum points. A horizontal length of around 10% was also independently found by both Kroo and Gage to be an optimum point [4,7]. It also can be observed that increasing the vertical length above 35% and the horizontal length above 15% only decreases the aerodynamic performance of the wing.

Chapter 5. Conclusions

The final chapter will discuss conclusions obtained from the results seen in Chapter 3 and 4, and future work recommendations.

5.1 Conclusions

This research aimed to investigate the aerodynamic performances of C-wings and to better understand how changing the geometry of the C-wing affects its performance. This research looked at the performance of the C-wing when airspeeds were less then Mach 0.3. A few of the overall conclusions drawn from the results include the following. When the vertical section of the C-wing is held constant and the horizontal section changes, the coefficient of lift and the lift-to-drag ratio decrease linearly, and the coefficient of drag increases linearly. When the horizontal section of the C-wing is held constant and the vertical section is changed, the coefficient of lift and the lift-to-drag ratio decrease linearly. The coefficient of drag initially increases then begins to decrease once the vertical length increases beyond 16.67%. It was discovered that there is a local maximum point for a C-wing when its vertical length is between 12-17% and its horizontal length is less than 12%. It was also observed that the aerodynamic performance of the C-wing increased slightly as the sweep angle of the vertical section was increased. Finally, it was concluded from Figure 27 that the C-wing could be potentially used as a control device for an aircraft with little affect to the aerodynamic lift and drag performance.

5.2 Future Work Recommendations

The results from this research only considered inviscid air flow. A good continuation of this research would be the comparison of the results with viscous flow simulations and experimental testing. Viscous flow simulations and experimental testing would permit a more accurate analysis of the specific magnitude change the C-wing has on the coefficient of lift and drag and the lift-to-drag ratio. It would also provide a better understanding of what C-wing geometry configurations give local, and possibly global, optimum points. Another good continuation of this research would be to do a more in-depth study of dynamically changing the sweep angle of the wings as means to control the aircraft.

References

[1] *FAA AEROSPACE FORECAST Fiscal years 2019-2039.* faa.gov (2019) Web 1/23/2020

[2] Anderson, John D. *Introduction to Flight*. 8th ed., McGraw-Hill, 2016.

[3] Raymer, Danial P. *Aircraft design: A Conceptual Approach.* 2nd ed, American Institution of Aeronautics and Astronautics, 1992

[4] Kroo, Iian, McMasters, John, Smith, Stephen, *Highly Nonplanar Lifting Systems.* NASA, 1995 "Transportation Beyond 2000: Technologies Needed for Engineering Design"; p.331-370; NASA-CP-10184-Pt-1

[5] Bertin, John J., Cummings, Russell M. *Aerodynamics for Engineers*. 5th ed., Pearson Prentice Hall, 2009.

[6] Anderson, John D. *Fundamentals of Aerodynamics*. 6th ed., Mcgraw-Hill, 2017.

[7] Gage, Peter J, *New Approaches to Optimization in Aerospace Conceptual Design*. NASA, 1995; NASA-CR-196695, A-950044, NAS 1.26196695

[8] Abbott, Ira H., Von Doenhoff, Albert E., *Theory of wing sections.* Dover Publications, 1999